Published in final edited form as:

Neuron. 2023 December 20; 111(24): 3988–4005.e11. doi:10.1016/j.neuron.2023.09.014.

Species-specific FMRP regulation of RACK1 is critical for prenatal cortical development

Minjie Shen[1,2,12,13], **Carissa L. Sirois**[1,2,12], **Yu Guo**[1,2,12], **Meng Li**[1,2,12,14], **Qiping Dong**[1], **Natasha M. Méndez-Albelo**[1,2,3], **Yu Gao**[1,2], **Saniya Khullar**[1,4], **Lee Kissel**[5], **Soraya O. Sandoval**[1,2,5], **Natalie E. Wolkoff**[1,2], **Sabrina X. Huang**[1,2], **Zhiyan Xu**[1,2,6], **Jonathan E. Bryan**[1,4], **Amaya M. Contractor**[1,2], **Tomer Korabelnikov**[1,2], **Ian A. Glass**[7], **Dan Doherty**[7], **Birth Defects Research Laboratory**[7], **Jon E. Levine**[2,8], **André M. M. Sousa**[1,2], **Qiang Chang**[1,9,10], **Anita Bhattacharyya**[1,11], **Daifeng Wang**[1,4], **Donna M. Werling**[10], **Xinyu Zhao**[1,2,15,*]

[1]Waisman Center, University of Wisconsin-Madison, Madison, WI 53705, USA

[2]Department of Neuroscience, School of Medicine and Public Health, University of Wisconsin-Madison, Madison, WI 53705, USA

[3]Molecular Cellular Pharmacology Training Program, University of Wisconsin-Madison, Madison, WI 53705, USA

[4]Departments of Biostatistics and Medical Informatics, School of Medicine and Public Health, University of Wisconsin-Madison, Madison, WI 53705, USA

[5]Neuroscience Training Program, University of Wisconsin-Madison, Madison, WI 53705, USA

[6]Graduate Program in Cell and Molecular Biology, University of Wisconsin-Madison, Madison, WI 53705, USA

[7]Birth Defects Research Laboratory, University of Washington, Seattle, WA 98195, USA

[8]Wisconsin National Primate Research Center, University of Wisconsin-Madison, Madison, WI 53715, USA

[*]Correspondence: xinyu.zhao@wisc.edu.

CONSORTIA:

The members of the Birth Defects Research Laboratory (BDRL) are Ian A. Glass, Ian G. Phelps, Jennifer C. Dempsey, Kevin Lee, Lucy Cort, Kimberly A. Aldinger, and Dan Doherty.

AUTHOR CONTRIBUTIONS

X.Z. conceived the concept, designed experiments, wrote the manuscript, and secured funding. M.S., C.L.S., Y.Guo., and M.L. designed experiments, collected data and wrote the manuscript. M.S., A.M.M.S, Y.Gao, and Q.D. generated cortical slice data. N.M.M-A, S.O.S., A.C., N.W., T.K., Z.X., and S.X.H. collected data. A.B. rederived the FX08 iPSC line; D.M.W. and L.K. performed gene set enrichment analyses for ASD and ND genes; Q.D. and Q.C. performed patch-clamp analyses. D.W., S.K., and J.E.B. performed gene ontology and correlation analysis; I.A.G, D.D., and BDRL contributed to human cortical slice study; J.E.L. contributed to rhesus macaque study.

DECLARATION OF INTERESTS

The authors declare no competing interests.

SUPPLEMENTAL INFORMATION

There are 7 supplemental figures and 3 supplemental Tables (Table S2, Table S4, Table S7) in the Supplemental Information file. There are addition 4 supplemental tables:

[9]Department of Neurology, School of Medicine and Public Health, University of Wisconsin-Madison, Madison, WI 53705, USA

[10]Laboratory of Genetics, University of Wisconsin-Madison, Madison, WI 53706, USA

[11]Department of Cell and Regenerative Biology, School of Medicine and Public Health, University of Wisconsin-Madison, Madison, WI 53705, USA

[12]These authors contributed equally

[13]Present address: The State Key Laboratory of Medical Neurobiology, MOE Frontiers Center for Brain Science, and the Institutes of Brain Science, Fudan University, Shanghai 200032, China

[14]Present address: Jiangsu Key Laboratory of Brain Disease and Bioinformation, Research Center for Biochemistry and Molecular Biology, Xuzhou Medical University, Xuzhou 221000, China.

[15]Lead contact

SUMMARY

Fragile X messenger ribonucleoprotein 1 protein (FMRP) deficiency leads to fragile X syndrome (FXS), an autism spectrum disorder. The role of FMRP in prenatal human brain development remains unclear. Here we show that FMRP is important for human and macaque prenatal brain development. Both FMRP-deficient neurons in human fetal cortical slices and FXS patient stem cell-derived neurons exhibit mitochondrial dysfunctions and hyperexcitability. Using multiomics analyses, we have identified both FMRP-bound mRNAs and FMRP-interacting proteins in human neurons and unveiled a previously unknown role of FMRP in regulating essential genes during human prenatal development. We demonstrate that FMRP interaction with CNOT1 maintains the levels of receptor for activated C kinase 1 (RACK1), a species-specific FMRP target. Genetic reduction of RACK1 leads to both mitochondrial dysfunctions and hyperexcitability, resembling FXS neurons. Finally, enhancing mitochondrial functions rescues deficits of FMRP-deficient cortical neurons during prenatal development, demonstrating targeting mitochondrial dysfunction as a potential treatment.

Graphical Abstract

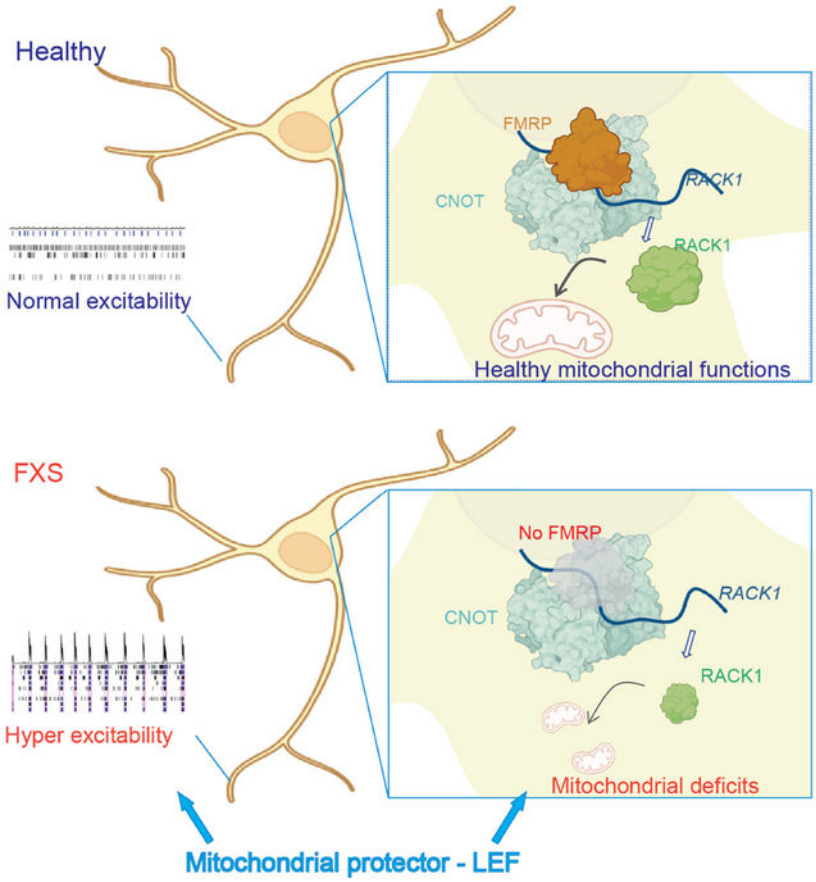

eTOC Blurb

Shen et al demonstrate that FMRP is critical for prenatal human brain development through regulating mitochondrial functions. They discovered that FMRP interacts with other proteins to regulate genes important for neuronal development. They show that enhancing mitochondrial functions rescues hyperexcitability of human fragile X syndrome patient derived neurons.

Keywords

FMRP; *FMR1* ; fragile X syndrome; human-specific; prenatal development; mitochondria; CLIP-seq; FMRP interactor; RACK1; CNOT1; mass spectrometry; hyperexcitability; MEA; physiology; pluripotent stem cells; *ex vivo* cortical slices; macaque

INTRODUCTION

Mitochondrial deficits are associated with both psychiatric and neurodevelopmental disorders (NDD), including autism spectrum disorders (ASD)[1–3]. However, how mitochondrial functions are regulated during human brain development and how their dysregulation contributes to NDD are unknown. Fragile X messenger ribonucleoprotein 1 protein (FMRP) is a brain-enriched RNA binding protein, and its deficiency leads to fragile X syndrome (FXS). FXS is the most common heritable cause of intellectual disability,

impacting 1 in 4,000 males and 1 in 6,000 females and is also the most common single-gene cause of ASD[4–6]. Despite extensive effort, how FMRP deficiency impairs neurodevelopment remains unclear. We have previously demonstrated that FMRP deficiency causes reduced mitochondrial fusion leading to mitochondrial fragmentation in mouse neurons, and that enhancing mitochondrial fusion rescues behavioral deficits of *Fmr1* knockout mice[7], which have been confirmed by subsequent studies[8–13]. However, unsuccessful FXS clinical trials[14] and differences between human and animal genetics[15] underscore the importance of investigation of human-specific FMRP targets for understanding FXS and ASD, disorders affecting higher brain functions[16]. Whether mitochondrial dysfunction plays a role in human FXS, and whether this dysfunction is evident during early prenatal development, remains unknown.

FMRP is expressed in both neural progenitor cells and neurons of the mammalian neocortex from prenatal development to adults[17,18]. Studies using animal models and transcriptomics analysis of postmortem human cortical tissue have shown that the levels of *FMR1* mRNA and FMRP protein increase significantly after birth and continues to adulthood[18,19], supporting a well-known role of FMRP in promoting neuronal maturation and synaptogenesis during postnatal brain development[17,20]. On the other hand, studies have shown that FMRP deficiency also affects mouse cortical development including radial glial differentiation, neuronal morphogenesis, and cortical neuron distribution[18,21]. Studies using human pluripotent stem cell (hPSC) derived neurons have demonstrated that FMRP-deficient human neurons exhibit altered neuronal production, impaired morphogenesis, and hyper excitability[16,22], suggesting that FMRP plays important roles in human prenatal development. However, how FMRP deficiency affects human prenatal brain development remains unknown.

Genome-wide binding studies have identified a large number of FMRP-bound mRNAs in juvenile mouse brains and postmortem adult human brains, as well as immature neural progenitors and neurons[17]. We have shown that FMRP has cell type-specific targets and its deficiency can lead to both increased and decreased protein and mRNA levels[23,24]. A major question that remains is how FMRP exerts cell type and target specificity. It is hypothesized that FMRP may act through interacting with its protein co-factors[17]. However, no study to date has identified FMRP-interacting proteins in human neurons.

Here, we tested the hypothesis that FMRP maintains neuronal mitochondrial functions during human prenatal development through regulating essential genes and that targeting mitochondria can correct neuronal deficits. We show that FMRP is critical for human prenatal brain development and that this role is conserved in macaques. Both FXS patient stem cell-derived neurons and FMRP-deficient neurons in human fetal cortical slices exhibit impaired mitochondrial functions and hyperexcitability. Using crosslink immunoprecipitation followed by either transcriptomic or proteomic analyses, we have identified both FMRP-bound mRNAs and FMRP-interacting proteins in human neurons and unveiled a previously unknown role of FMRP in regulating essential genes during human prenatal development. Many of these genes have been associated with ASD and NDD[25]. We further demonstrate that FMRP interaction with CNOT1 maintains the expression levels of receptor for activated C kinase 1 (RACK1), a human-specific FMRP target.

RACK1 knockdown leads to both mitochondrial dysfunctions and hyperexcitability in human neurons, resembling FXS neurons. Finally, we screened mitochondrial enhancing compounds that could rescue deficits of human FXS neurons and showed that leflunomide, an FDA-approved drug for rheumatoid arthritis, rescues hyperexcitability phenotypes of FXS human neurons *in vitro* and *ex vivo*. Our data unveil a role of FMRP in human prenatal brain development and demonstrate targeting mitochondrial dysfunction as a potential treatment.

RESULTS

Human FMRP-deficient developing neurons exhibit mitochondrial deficits and hyperexcitability

To investigate whether FMRP deficiency affects neuronal mitochondria during human cortical development, we generated organotypic slices from postmortem mid-fetal human cortical tissue (postconceptional weeks 14–17) and infected slices lentivirus (LV) to knock down FMR1 (LV-*shFMR1*-mCherry)[22] and to target mitochondria (LV-*syn-mitoGFP*)[7] (Figures 1A–B, Figures S1A–S1B, Table S1) We observed that the proximal dendrites of LV-*shFMR1*-infected neurons had more fragmented mitochondria (reduced aspect ratio, Figures 1C and 1D) and reduced amount (area, Figure 1E) of mitochondria, as well as increased oxidative stress, measured by the levels of oxidative stress products nitrotyrosine (NT, Figures 1F and 1G) and 8-oxoguanine (8-oxoG, Figure S1D–S1E), compared to controls. In addition, we observed similarly altered mitochondrial morphology and dysfunction in LV-*shFMR1*-infected neurons in mid-fetal cortical slices of rhesus macaque (Figure S1C, Figures 1H–1L), suggesting that FMRP regulation of mitochondrial function is conserved in primates. Whole-cell recordings showed that LV-*shFMR1*-infected neurons exhibited significantly more positive resting membrane potential (RMP, Figures 1M–1O) and increased input resistance ($R_{in,}$ Figure 1P), suggesting an increased excitability of LV-*shFMR1* infected neurons. Taken together, our data show that FMRP deficiency leads to mitochondrial deficits and hyper excitability in human neurons during prenatal development.

To determine whether FMRP deficiency affects mitochondrial functions in human FXS neurons, we generated new FXS patient-derived induced pluripotent stem cells (iPSCs) from a published FXS patient (FXS-1, or FXS)[26] (Figures S2A–S2C). These FXS iPSCs and healthy control (Ctrl-1, or Ctrl) iPSCs[27] were readily differentiated into dorsal forebrain excitatory neurons using an established method[24]. We differentiated this FXS and additional FXS lines[24,26], as well as a *FMR1* gene deleted (KO) line[24] and their controls[7] into dorsal forebrain neurons for 4 weeks (Figure 2A, Figures S2D–S2F). We observed that mitochondria in FMRP-deficient neurons had reduced aspect ratio (Figures 2B and 2C, Figures S2G and S2H), reduced total area (Figure 2D), elevated oxidative stress levels (Figure 2E, Figures S2I and S2J), and reduced mitochondrial membrane potential (MMP, Figures 2F–2G) compared to Ctrl neurons. To further assess mitochondrial function, we measured cellular ATP levels, as well as NAD and NADH levels, in the presence of carbonyl cyanide4-(trifluoromethoxy)phenylhydrazone (FCCP). FCCP decouples ATP production from the mitochondrial electron transport chain leading to reduced ATP production and is widely used to study mitochondrial functions[28]. Although the baseline

levels of either ATP or NAD and NADH were not significantly different between FXS and control neurons (p=0.8), control neurons exhibited reduced ATP levels and reduced NAD and NADH levels, in response to FCCP, whereas FXS neurons failed to respond to FCCP treatment (Figure S2K–S2L). Furthermore, FXS neurons exhibited hyperexcitability measured using multielectrode arrays (MEAs) (Figures 2H–M, Figures S2M–S2N, Table S2), a physiological phenotype reported previously in FXS iPSC-derived neurons[22,29]. Therefore, FMRP deficiency leads to mitochondrial deficits and hyperexcitability in developing human neurons.

FMRP regulates genes critical for neuronal development in humans

We then assessed genes that regulate mitochondrial biogenesis and dynamics, and found that human FXS neurons had reduced levels of mitochondrial biogenesis gene *PPARGC1A* (Peroxisome proliferator-activated receptor gamma coactivator 1-alpha or PGC-1-alpha) and mitochondrial fusion genes (*MFN1)* (Mitofusion 1) and *OPA1*, but increased levels of mitochondrial fission gene *FIS1*, compared to controls (Figure S2O). However, none of them have been identified as FMRP-bound targets in human neural progenitor cells (NPCs) or immature (1-week differentiation) neurons in our published crosslinking-immunoprecipitation followed by next generation sequencing (CLIP-seq) study[24]. To understand how FMRP deficiency leads to these widespread changes in mitochondrial genes and functions in mature human neurons during prenatal development, we differentiated three hPSC lines with endogenous FLAG tagged FMRP[24] and their isogenic controls (parental PSC lines without FLAG tag) (Table S1) to neurons for 8 weeks and performed CLIP-seq using our published protocol[24] (Figure 3A). We identified 36 high confidence FMRP-bound mRNAs in human mature neurons (Table S3).

Gene set enrichment analysis[30,31] showed that FMRP-bound mRNAs were enriched in pathways involved in early developmental processes including cellular component morphogenesis, cell morphogenesis involved in neuron differentiation, cytoskeletal protein binding, microtubule binding, axon guidance, and neuron projection (Figure 3B, Figure S3A). We compared to published sets of ASD and NDD risk genes[32–35] and found that FMRP targets exhibited significant enrichment for both ASD[32] and NDD[33] risk gene sets (ASD odds ratio for enrichment =21.7, Bonferroni-adjusted P=3.7e-4; NDD OR=17.0, P_{adj}=3.1e-08; Figure 3C; Table S3). Additionally, FMRP targets exhibited significant enrichment in neuronal-associated modules[36] with reduced, but not elevated, expression in the ASD brain (M4: OR=10.6, P_{adj}=1.2e-03; M10: OR=5.7, P_{adj}=0.12, M16 OR:=9.2, P_{adj}=2.3e-03) (Figure 3D; Table S3).

We compared our FMRP targets in human mature neurons with our previously identified FMRP targets in human NPCs and immature (1-week differentiation) neurons[24] and found that mRNAs of 7 genes (*DPYSL2, HSP90AA1, HSP90AB1, RACK1, RPL4, TUBB2A*, and *ZNF91*) were bound by FMRP only in mature human neurons (Figure S3B), suggesting that these genes may play critical roles in more mature human neurons. We then further compared our mature neuron targets with published FMRP targets in juvenile mouse forebrain[37,38] and adult mouse hippocampal CA1 neurons[39]. Four FMRP targets, *HSP90AA1, RACK1, RPL4* and *ZNF91*, are specific to mature human neurons (Figure 3E).

We performed RNA immunoprecipitation followed by quantitative PCR (RNA IP-qPCR) on independent collections of human FLAG-FMRP neurons. FLAG antibody pulled down *HSP90AA1, RACK1, RPL4*, and *ZNF91* mRNA in FLAG-FMRP neurons, but not from isogenic control neurons (Figure S3C–F). Then, using an antibody against FMRP[22], we found that FMRP bound *RACK1* and *HSP90AA1* mRNAs but not *RPL4* or *ZNF91* mRNAs in human midfetal cortical tissue (Figure 3F, Figure S3G–J). On the other hand, none of these mRNAs showed significant enrichment in FMRP RNA-IP in either macaque or mouse brain tissue, whereas positive control MAP1B mRNA[22] showed enrichment (Figure S3K). Therefore, FMRP binds a subset of mRNAs in human mature neurons and some of these targets are specific to human mature neurons and exhibit species specificity.

Reduced RACK1 levels leads to mitochondrial deficits and hyperexcitability

We next determined which FMRP targets are directly involved in mitochondrial dysfunction and hyperexcitability. Because FMRP deficiency affects gene expression levels in both directions[23], we proposed two models. In Model 1, an FMRP target (Target X) exhibits reduced expression levels in FXS and therefore knocking down of Target X in healthy neurons should lead to both neuronal hyperexcitability and mitochondrial deficits. In Model 2, Target X exhibits increased expression levels in FXS, therefore knockdown of Target X should lead to both neuronal hypo-excitability and mitochondrial deficits. We selected 12 targets involved in cellular pathways affecting mitochondrial functions and found that knocking down of 8 targets individually (*ATP5B, DYNC1H1, KIF5C, HSP90AA1, SPTAN1, CRMP1, CLTC*, and *RACK1*) led to neuronal hyperexcitability, knocking down of 1 target (MAP2) led to hypoexcitability, and knocking down of the other 3 genes (*HSP90AB1, SPTBN1*, and *PRPF8*) exhibited no consistent effect (Figures S4, Table S4). The protein expression levels of CRMP1, PRPF8, and RACK1 protein levels were lower, whereas ATP5B protein levels were higher, while the other 8 proteins showed no significant changes in FXS neurons compared to Ctrl neurons (Figures S4). Therefore, CRMP1 and RACK1 were the two FMRP targets whose expression levels were reduced in FXS neurons and their knockdown in Ctrl neurons led to hyperexcitability, thus fitting our Model 1.

We further confirmed that both mRNA and protein levels of RACK1 were significantly reduced in FXS neurons and FMRP-deficient neurons in *ex vivo* human fetal cortical slices, compared to controls (Figures 4A–4D, S5A). In addition, knockdown of *RACK1*, but not *CRMP1*, *DYNC1H1*, or *SPTBN1*, led to significantly reduced MMP in human PSC-differentiated neurons (Figures 4F and 4G, Figure S5B–S5C). Therefore, FMRP maintains the expression levels of RACK1, a human mature neuron-specific target of FMRP, and RACK1 deficiency leads to both mitochondrial dysfunctions and neuronal hyperexcitability resembling FXS neurons.

RACK1 is a scaffolding protein with emerging roles in regulating multiple cellular functions including cellular metabolism and stress responses[40]. Reduced RACK1 levels have been found in neurodegeneration[41]. The levels of *RACK1* mRNA are significantly higher in prenatal brain compared to the postnatal period[19], especially in the medial frontal cortex (MFC)[42] implicated in both FXS and ASD[43]. However, the function of RACK1 in human cortical development remains unclear. We observed that neurons with *RACK1* knockdown

(*shRACK1*) exhibited reduced expression of genes important for mitochondrial biogenesis (*PPARGC1A*/PGC1α) and fusion (*MFN1*), compared to controls (Figures S5D–S5J). In addition, neurons with *RACK1* knockdown exhibited reduced aspect ratio and reduced total mitochondrial area, without significant effect on NT levels (Figure 4H–K), but reduced responses to FCCP treatment on ATP production and NAD/NADH levels compared with controls (*shNC*) (Figure S5K–S5L). Furthermore, *RACK1* knockdown led to increased hyperexcitability in hPSC differentiated neurons (Figures 4L–4P). Therefore, knocking down *RACK1* in control neurons recapitulates the phenotypes of FXS neurons.

We then expressed exogenous RACK1 using LV (Figure S5M). LV-RACK1-infected FXS neurons (RACK1-BFP+) exhibited increased MMP and reduced hyperexcitability compared to adjacent non-infected neurons in the same dish (LV-RACK1-BFP-) or control LV (LV-BFP)-infected neurons (Ctrl-BFP+) (Figure 4Q–4W). These data demonstrate that RACK1 is necessary for proper mitochondrial function and excitability of developing human neurons and reduced RACK1 levels contribute to the deficits of FXS neurons.

FMRP interacts with CNOT1 and regulates *RACK1* mRNA levels

Although FMRP is known to be a translational repressor, its deficiency also affects mRNA expression, either directly or indirectly[17]. How FMRP directly regulates mRNA levels of its targets is unclear. We performed co-immunoprecipitation (Co-IP) followed by mass spectroscopy of neurons differentiated from FMRP-FLAG hPSCs[24] and identified 56 FMRP interactors (Table S5). These FMRP interactors are enriched for proteins involved in regulation of translation, stress granule assembly, and metabolism of RNA (Figure 5A), as well as high association to FXS pathology (Figure S6A).

FMRP targets (CLIP) and FMRP interactors (Co-IP) demonstrated strong enrichments for genes with “falling” trajectories (lower expression in postnatal than prenatal development[25]) (CLIP: OR=3.2, p_{adj}=4.3e-03; Co-IP: OR=2.2, p_{adj}=0.0495; FET; Table S3 and Table S6). This contrasts with FMRP targets in adult human brains[44] and juvenile mouse brains[37], which instead preferentially show “rising” trajectories (higher expression in postnatal than prenatal development) (mouse rising OR=1.6, P_{adj}=9.4e-09, falling OR=0.97, P_{adj}=1; human rising OR=1.4, P_{adj}=1.1e-12, falling OR=1.0, P_{adj}=1; Table S3 and Table S6). “Falling” genes are enriched for highly constrained genes which are intolerant to loss-of-function mutations (haploinsufficient)[25], and so are thought to drive critical functions in prenatal development (Figures 5B–5C). In line with this pattern, both our FMRP targets and FMRP interactors also demonstrated substantial enrichment for highly sequence-constrained genes, with 20 of the 36 CLIP targets (55.6%), and 28 of the 56 Co-IP interactors (50%) reported to have a probability of loss-of-function intolerance (pLI) score[45] ≥ 0.995 (CLIP: OR=15.8, P_{adj}=2.3e-13, median pLI for all targets = 0.998; Co-IP: OR=11.5, P_{adj}=4.7e-16, median pLI for all interactors = 0.996; FET; Tables S5).

We then performed agglomerative hierarchical clustering and compared correlation between FMRP targets (CLIP) genes with FMRP interactors (Co-IP) genes based on their dynamic expression patterns in the human MFC from early fetal to late midfetal development[19]. (Figure S6B). Surprisingly, although FMRP positively regulates RACK1 mRNA and protein levels (Figures 4A–4D, Figure S5A), the expression levels of *FMR1* exhibited no correlation

with *RACK1*. On the other hand, the mRNAs of 31 FMRP interactors exhibited positive correlation with *RACK1*, among which were *CNOT1* implicated in ASD[46] and 10 genes whose protein products interact with CNOT1 ("CNOT1 interactors") (Figure S6C). Both CNOT1 and CNOT7 are core components of CCR4-NOT RNA regulatory protein complex known for carrying out mRNA decay[47]. Hence, our data indicate that FMRP has an essential and previously unknown role in prenatal human brain development. The positive correlation between *RACK1* and *CNOT1*, both essential genes for humans (PLI=1.0)[45], suggest that CNOT1 may regulate RACK1 expression.

Our hypothesis is that during embryonic development, FMRP's interaction with CNOT1 is important in maintaining the expression of essential genes for neuronal development, such as *RACK1* (Figure 5D). We performed Co-IP on HEK293 cells transfected with FLAG-FMRP and confirmed that FLAG-FMRP pulled down endogenous CNOT1 protein (Figure S6D). We then confirmed that endogenous FMRP directly interacts with endogenous CNOT1 protein in human neurons (Figure 5E). In addition, using proximity ligation assays (PLAs), which allows for the detection of protein-protein interactions *in situ*[48], we confirmed that CNOT1 and FMRP proteins indeed interact in human neurons (Figure 5F) and CNOT1 bound *RACK1* mRNA in human mid-fetal cortical tissue (Figures 5G). Down-regulation of CNOT1, but not CNOT7, diminished binding of FMRP to *RACK1* mRNA (Figure 5H). In addition, knocking down either FMRP or CNOT1 also diminished binding of CNOT1 to *RACK1* mRNA (Figure 5I). Furthermore, *RACK1* mRNA had a reduced half-life ($T_{1/2}$) in both FMRP-deficient cells (2.62 h) and CNOT1-deficient cells (3.07 h) compared to control cells (5.22 h; Figure 5J). Hence, both FMRP and CNOT1 maintain *RACK1* mRNA stability. The *CNOT1* mRNA levels did not show significant change in FXS neurons (Figure S6E). CNOT1 knockdown had no significant effect on MMP or sensitivity to FCCP in ATP production (Figure S6F–S6G). Hence, our data suggest that FMRP and CNOT1 facilitate each other's binding to *RACK1* mRNA and the binding by both FMRP and CNOT1 maintains the stability of *RACK1* mRNAs in developing human neurons.

Mitochondrial protector corrects hyperexcitability of FMRP-deficient human neurons

We next investigated whether enhancing mitochondrial functions could rescue deficits of human FXS human. We first assessed 17 FDA-approved drugs and natural products that could potentially enhance mitochondrial functions, as well as M1, the MFN1 and MFN2 activator we tested on *Fmr1*-KO mouse neurons[7]. Noticeably, 12 of 18 mitochondrial protectors, but not M1, restored MMP deficits in FXS neurons after a 24-hour of treatment (Table S7). We then selected several compounds based on their efficacy, safety, and accessibility. Only leflunomide showed consistent elevation of MMP and reduction of hyperexcitability in FXS neurons (Table S7).

Leflunomide (LEF) is an anti-inflammatory drug approved to treat rheumatoid arthritis[49]. Although its mechanisms of action remain unclear, leflunomide has been shown to activate *MFN1* and *MFN2* gene expression in mammalian cells[50–52]. Leflunomide had no significant effect on mRNA levels or protein levels of RACK1 and CNOT1 in control or FXS neurons (Figure 6A, Table S7, Figure S7A–S7H). In addition, leflunomide did not significantly affect interaction between FMRP and CNOT1 (Figure S7I–S7K), nor FMRP binding

to *RACK1* mRNA (Figure S7L). Furthermore, leflunomide did not show toxicity nor a significant effect on mitochondrial shape, amount, or cellular NT levels in human neurons ($P>0.05$). We then treated FXS neurons and observed that leflunomide treatment rescued mitochondrial shape (Figures 6B and 6C) and amount (Figure 6D), without significant effects on neuronal oxidative stress (Figure 6E). Leflunomide treatment also rescued reduced MMP levels in FXS neurons, without significant effect on control neurons (Figure 6F–6I). In addition, leflunomide increased the levels of *PPARGC1A* and *MFN2* mRNA levels in FXS neurons (Figure S7M–S7Q). Furthermore, leflunomide also rescued the responses of FXS neurons to FCCP (Figure S7R–S7S). Finally, leflunomide treatment significantly alleviated hyperexcitability of FXS neurons assessed at 4, 5, and 6 weeks post-plating (Figures 6J–6P; Figure S7T–S7AB).

We then treated human fetal cortical slices with FMRP knockdown (*shFMR1*) (Figure 7A). We observed that leflunomide had no significant effect on control (*shNC*) neurons but led to increased mitochondrial amount and reduced oxidative stress levels, without significant effect on mitochondrial shape, in FMRP-deficient (*shFMR1)* human neurons in the cortical tissue (Figures 7B–7I). In addition, leflunomide significantly increased resting membrane potential and reduced input resistance of FMRP-deficient neurons in human fetal cortex (Figures 7J–7L). Therefore, our data support that enhancing mitochondrial functions may correct neuronal deficits resulting from FMRP deficiency in human neurons.

DISCUSSION

We have demonstrated that FMRP is essential for maintaining mitochondrial functions during human prenatal development by regulating genes whose expression is highest during the early prenatal periods of neurodevelopment (e.g. *RACK1*) and whose loss of function contributes to neurodevelopmental disorders, including ASD[25]. Since neurons rely on mitochondria over glycolysis for energy, even minor reductions in mitochondrial function can have significant and profound implications. However, a direct link between mitochondrial deficits and autism is largely lacking[53]. Studies from our and other laboratories have demonstrated mitochondrial dysfunctions in animal models of FXS[8–12]. Here, we provide evidence for a significant role of FMRP in mitochondrial functions in developing human neurons and highlight the importance of species-specific mechanisms.

FMRP protein and mRNA are expressed in the mammalian neocortex from prenatal development to adulthood with increased levels after birth into adulthood[17–19], supporting the role of FMRP in neuronal maturation and synaptic plasticity in postnatal brains[17,20]. Limited studies have investigated FMRP function in mouse cortical development[18,21]. Our data show that FMRP targeted genes are not only are enriched with genes implicated in ASD[17,24,37–39,44] but also exhibit convergence during human mid-fetal brain development[25,43]. Although hPSC-differentiated neurons provide important model systems for studying human brain development[16], they cannot fully represent the complex, three-dimensional structure of the developing human brain. Our use of *ex vivo* brain slices from human fetal cortex provide a much-needed missing link between cell culture and *in vivo* brains. Importantly, our results from *ex vivo* brain slices show that such function of FMRP is

conserved in rhesus macaque, providing a basis for future studies using non-human primate models for FXS and ASD research.

FXS clinical trials based on mouse studies have not yielded effective treatment[14]. Advancements in genomics have identified gene expression signatures that are unique to humans and nonhuman primates[15]. Identification of human-specific FMRP targets and investigation of their functional significance are critical for understanding FXS and ASD, disorders affecting higher brain functions[16], however such investigation is scarce[54]. We have identified *RACK1* as a FMRP mRNA target in human PSC-differentiated mature neurons and midfetal cortical brain tissue, which has not been previously identified in either postmortem adult human brains[44] or human PSC differentiated immature brain organoids[55], suggesting that RACK1 is a developmental stage specific target of FMRP. RACK1 is a protein that has seven conserved tryptophan-aspartate repeat domains[56]. These proteins have diverse functions but share a common role in serving as hubs for protein-protein interactions for cellular signaling events[56]. Although originally identified as an anchoring protein for protein kinase C, RACK1 has been shown to regulate many cellular processes, including protein translation, localization, trafficking, and activation[40]. Although RACK1 has been implicated in metabolism in cancer cells[57], the role of RACK1 in mitochondrial functions in neurons had not been assessed. Our data demonstrate that RACK1 is important for maintaining mitochondrial functions and reduced RACK1 expression is likely one of the reasons for mitochondrial deficits found in human FXS neurons. Since FMRP does not bind *RACK1* mRNA in either midfetal macaque or neonate mouse cortical tissues, FMRP regulation of RACK1 is species-specific. It would be interesting and important to investigate in the future whether RACK1 may contribute to species differences of FMRP functions.

We have shown that FMRP has cell type-specific targets[24] and that FMRP deficiency can lead to upregulation of some genes but down regulation of other genes[23,24]. It remains unclear how FMRP exerts cell type and target specificity and whether protein interactors of FMRP may facilitate these functions[17]. Our Co-IP identification of FMRP interacting proteins unveiled the interaction between FMRP and CNOT1, the core scaffold protein of the CCR4-NOT RNA regulatory complex. An unexpected observation is that CNOT1 knockdown led to reduced *RACK1* mRNA stability, because CCR4-NOT complex is known to activate mRNA decay[47]. Like RACK1, CNOT1 is also an essential gene for humans (pLI=1.0)[45]. It is possible that CNOT1 acts independently of CCR4-NOT complex and maintains mRNA stability in specific cell types and during specific developmental stages, a function that should be further investigated in future studies.

Since our initial report on mitochondrial fusion deficits in FMRP-deficient mouse neurons[7], subsequent studies have provided additional evidence and mechanisms for mitochondrial dysfunction in neurons and astrocytes of FXS mouse models[8–13,58–60]. While these studies provide strong evidence for important roles of FMRP in regulating mitochondrial functions, supporting the initial observations made in Drosophila *dFmr1* mutants[61] and *Fmr1*-KO mice[7], they have also revealed the complexity of mitochondrial regulation and cell type-, developmental stage-, and assay specific-functions of FMRP. For example, we have shown increased mitochondrial fragmentation in both *Fmr1*-KO mouse[7] and FXS human neurons, which are supported by several studies[12,13,62]. However, Bulow et al observed larger surface

area of mitochondria in the dendrites and longer mitochondria in axon initial segment of *Fmr1*-KO mouse neurons in an activity-deprived model for studying homeostatic plasticity[8]. The main function of mitochondria is the production of ATP. Although reduced ATP levels have been found in the brains of juvenile (postnatal day 21, or P21) and 12-month-old *Fmr1*-KO mice[10] and in cultured *Fmr1*-KO neonatal hippocampal neurons[12], ATP levels are not significantly changed in young (P10) *Fmr1*-KO mouse brains[11]. Since we did not observe significant differences in ATP levels between FXS and control human neurons, we further investigated mitochondrial functions in FXS neurons by assessing cellular ATP levels as well as NAD and NADH levels respond to the mitochondrial decoupler FCCP. FXS neurons failed to show reduced ATP levels in response to FCCP, whereas control neurons responded readily. It is possible that FXS neurons may have increased proton leak, as previously found in *Fmr1*-KO mouse neurons and human fibroblasts[11,12]. Therefore, FXS neurons were not sensitive to mitochondrial decoupler FCCP treatment. Because human neurons are sensitive to high concentrations of FCCP, it is not possible to test whether FXS neurons may respond to increased amount of decoupling. The fact that RACK1-deficient human neurons also lost sensitivity to FCCP further supports the role of RACK1 in mediating FMRP regulation of mitochondrial functions in human neurons. It will be interesting to determine whether inhibitors of proton leak may correct FXS human neurons as they did in mouse neurons[11,12]. Although both mouse and human neurons exhibit mitochondrial fragmentation, the reduced mitochondrial amount and reduced *PPARGC1A* expression levels seem to be unique to human FXS neurons and it will be important to further investigate this difference in future studies.

The most consistent phenotype of FMRP-deficient neurons in both mice and humans is reduced MMP[7,8,12,62]. MMP is critical for ATP production and mitochondrial functions, thus making this parameter a functional readout of mitochondrial state[28]. Fortunately, MMP assays are readily adaptable to high content imaging. To our surprise, M1 was not among the 12 compounds that enhanced MMP in human FXS neurons. This differential response between mouse and human neurons underscores the importance of studying human models for brain disorders[14]. Only leflunomide corrected both mitochondrial and neuronal excitability deficits of FXS neurons. Leflunomide was initially developed as an anti-inflammatory drug and has been approved to treat rheumatoid arthritis[49]. Although the mechanisms of actions are not fully clear, leflunomide has been shown to inhibit dihydroorotate dehydrogenase (DHODH), an inner mitochondrial membrane enzyme catalyzing de novo synthesis of pyrimidines[49]. In a chemical screen for transcriptional activators for the *MFN2* in Hela cells, leflunomide was identified as the top compound that can activate *MFN1* and *MFN2* gene expression and repress *DRP1* gene expression, without significant effect on *PPARGC1A* gene expression[50]. Leflunomide can increase mitochondrial fusion in several mammalian cell lines[50–52], but none of the cells were neurons. The effect of leflunomide on mitochondrial fusion in Hela cells occurs through the inhibition of DHODH and depends on MFN1/2[50]. We found that leflunomide increased *PPARGC1A* and *MFN2* mRNA levels, and leflunomide increased the amount of mitochondria in FXS neurons with only trend increase in mitochondria aspect ratio ($p=0.09$) in FMRP deficient neurons in human cortical tissue. These observations suggest that leflunomide may have more significant effect on mitochondrial production in human

neurons compared to Hela cells and mouse neurons. Our data suggest that action of leflunomide is likely independent of FMRP-*RACK1* regulation because leflunomide had no significant effect on FMRP-CNOT1 interaction, FMRP binding of *RACK1* mRNA, or *CNOT1* or *RACK1* expression levels in FXS or control neurons. It has also been shown that leflunomide may modify intracellular calcium signaling[63] and altered mitochondrial calcium homeostasis has been found in FMRP-deficient neurons[62]. How leflunomide increases *PPARGC1A* expression and whether inhibition of DHODH is involved in its rescue effect on FXS neurons will be an interesting future investigation.

In summary, we have demonstrated that FMRP deficiency leads to mitochondrial dysfunction and hyperexcitability in human neurons and that enhancing mitochondrial functions rescues FXS associated deficits. FMRP-regulated targets are highly enriched with genes implicated in ASD[17,37–39,44], as corroborated by this study. We propose that mitochondrial protector compounds may be promising therapeutics for human FXS and potentially ASD individuals.

STAR*METHODS

RESOURCE AVAILABILITY

Lead contact—Further information and requests for resources and reagents should be directed to and will be fulfilled by the Lead Contact, Prof. Xinyu Zhao (xinyu.zhao@wisc.edu).

Materials availability—Request for resources and reagents should be directed to the lead contact.

Data and code availability

- Data reported in this paper are available from the lead contact upon reasonable request.
- Raw and processed ChIP-seq data are deposited to Gene Expression Omnibus (GEO: GSE217284). This paper does not report original codes.
- Any additional information required to reanalyze the data reported in this paper is available from the lead contact upon reasonable request.

EXPERIMENTAL MODEL DETAILS

Human and macaque tissue—All work was performed according to NIH guidelines for the acquisition and distribution of human tissue for bio-medical research purposes and with approval by the Human Investigation Committees and Institutional Ethics Committees of each institute from which samples were obtained. De-identified postmortem human brain specimens (14 to 17 PCW) were obtained from the Birth Defects Research Laboratory (BDRL) at the University of Washington with ethics board approval and maternal written consent. This study was performed in accordance with ethical and legal guidelines of the University of Wisconsin-Madison Institutional Review Board. Appropriate informed consent was obtained and all available non-identifying information

was recorded for each specimen. Tissue was handled in accordance with ethical guidelines and regulations for the research use of human brain tissue set forth by the NIH (http://bioethics.od.nih.gov/humantissue.html) and the WMA Declaration of Helsinki (http://www.wma.net/en/30publications/10policies/b3/index.html). All experiments using non-human primates (91, 101 and 111 PCD) were carried out in accordance with a protocol approved by University of Wisconsin's Institutional Animal Care and Use Committee and NIH guidelines. All clinical histories, tissue specimens, and histological sections were evaluated to assess for signs of disease, injury, and gross anatomical and histological alterations. No obvious signs of neuropathological alterations were observed in any of the macaque specimens analyzed in this study.

See also Table S1. Cell lines and animal models used in this study.

***Ex vivo* fetal organotypic slice cultures, viral infection, and chemical treatment—**These procedures were performed as described[22,64]. Cortical walls from human and macaque brains at mid-gestation were dissected in Hibernate E solution (ThermoFisher, #A1247601) supplemented with 1X B27 (ThermoFisher 17504044), 1X Glutamax (ThermoFisher 35050061), and 1 X Penicillin-Streptomycin (ThermoFisher 15140122). Tissue was then imbedded in 3.2% low melting point agarose (American Bioanalytical) in PBS and sectioned in a Leica VT1200 S Vibrating blade microtome. After, they were transferred into ice-chilled artificial cerebrospinal fluid (ACSF; 125 mM NaCl, 2.5 mM KCl, 1.25 mM NaH2PO4, 1.0 mM MgCl2, 2.0 mM CaCl2, 25 mM NaHCO3, 25 mM dextrose, bubbled with 95% O2/5% CO2). 300 μm slices were transferred to 0.4 μm pore size, PET track-etched membrane, cell culture inserts (Falcon #353090; #353180) in BrainPhysTM Neuronal Medium (Stem Cell Technologies, #05790) supplemented with N2 (1:100), BDNF (25ng/mL), and B27 (1:50) as described[64]. At 1 day after plating or 1 day of in vitro culture (DIV1), 10 μl lentivirus (LV) (LV-*shFMR1*-EF1a-mCherry or LV-*shNC*-EF1a-mCherry, LV-hSyn-Mito-GFP) were added to 500 μl of culture medium per well. At DIV11, slices were collected for patch clamp recording or fixation for analysis. For drug treatment, 12.5 μM Leflunomide (Sigma-Aldrich, PHR1378) or DMSO as vehicle was administered on DIV 10 for 24 hours, prior to patch clamp recording or fixation for analysis.

Generation and culturing of a new human pluripotent stem cell line from FXS patient—The FXS patient (FX08) iPSC line (FXS or FXS-1) was generated from previously published FXS skin fibroblasts[26] using Sendai non-integrating methods[27]. Briefly, reprogramming of fibroblasts was done using the Cytotune 2.0 kit (ThermoScientific, Catalog #A16517) following the manufacturer's protocol. Cells were cultured on irradiated mouse embryonic fibroblasts (MEF) feeder layers (WiCell) with a daily change of hESC medium consisting of DMEM/F12 (Thermo Fisher Scientific), 20% knockout serum replacement (KSR, Thermo Fisher Scientific), 0.1 mM 2-mercaptoethanol (Sigma-Aldrich), 1x L-Glutamine (Thermo Fisher Scientific), and 6 ng/ml FGF-2 (Waisman Biomanufacturing Center). Individual reprogrammed colonies were picked and plated onto Matrigel for expansion and banking. iPSCs were stored in liquid N2. G-banding was performed by WiCell Cytogenetics Services (Madison, WI), as described previously[24,65].

Human PSC lines, maintenance, and neural differentiation—In addition to the new FXS (FXS-1) line (see above), we used several other human PSC lines, including three control iPSC lines: WC031i-5907–6 (Ctrl or Ctrl-1), WC032i-6007–1 (Ctrl-3)[27], GM00498–4 (Ctrl-2)[24], two other FXS iPSC lines": WC005i-FX11–7 (FXS-2) and WC007i-FX13–2 (FXS-3)[26], *FMR1* gene knockout (H1-KO)[24] and isogenic control (WA01 or H1) human embryonic stem cell (hESC) lines[66], H9 hESC (WA09) line[66], and our published FLAG tag knock-in human PSC lines (H1-FLAG, H13-FLAG, and GM1-FLAG)[24] and their corresponding isogenic controls (H1, H13 or WA13, and GM00498–4)[24,66]. (see new Table S1 for details). The above human PSC lines can be obtained through WiCell (https://www.wicell.org/), with appropriate MTA.

Before starting differentiation, hPSCs were thawed onto MEF feeder plates in hESC media containing 2x FGF and 10 μM ROCK inhibitor (Y-27632 dihydrochloride, Tocris). Cells were passaged every seven days onto new MEF plates using collagenase (1mg/ml in DMEM/F12) at a ratio of 1:3 to 1:6. Neural differentiation of human PSCs was carried out using our previously published dual SMAD inhibition-based protocol[7,22,24,65]. Briefly, neural differentiation was induced 5 days after passaging of hPSCs onto MEFs by switching from hESC medium to neural induction medium (NIM) consisting of DMEM/F12:Neurobasal 1:1, 1x N2, 1x L-Glutamine, 1x Anti-Anti (GIBCO), 10 μM SB432542 (Biogems), 100 nM LDN193189 (Selleck), and 5 μM XAV-939 (Selleck). Cells were cultured in NIM for 9 days with a daily medium change, with small molecules added fresh daily. Cells were then dissociated with TrypLE Express (Gibco) and re-plated 1:1 onto Matrigel-coated plates in neural progenitor cell (NPC) medium (Neurobasal medium, 1x L-glutamine,(Thermo Fisher Scientific), 1x N2, 0.5x B27 without vitamin A (Thermo Fisher Scientific), 1x Anti-Anti) supplemented with 10 μM ROCK inhibitor. Cells were maintained for 6 days with daily change of NPC medium, during which they transition from neuroepithelia to neural progenitors (NPCs) and reorganize into neural rosettes. At this stage NPCs were dissociated with Accutase (Thermo Fisher Scientific), frozen in NPC freeze medium (90% FBS, 10% DMSO), and stored in liquid N2. For experiments, NPCs were thawed onto Matrigel-coated plates in NPC medium plus 10 μM ROCK inhibitor such that surviving NPCs would be confluent after thaw. NPCs were either maintained in NPC medium for one day, or infected with LV expressing shRNA-BFP in NPC medium, then plated for experiments the following day (48 hours after thawing) onto either Matrigel-coated plastic plates or poly-L-ornithine and laminin-coated (poly-o/laminin) specialty plates (see information in subsequent sections). For all experiments, NPCs were plated at low density in NPC medium containing 10 μM ROCK inhibitor and 0.2 uM γ-Secretase Inhibitor XXI, Compound E (Calbiochem). The next day, plated cells were switched to neuron differentiation medium (NDM; Neurobasal medium, 1x GlutaMAX (Thermo Fisher Scientific), 1x Anti-anti, 1x N2, 0.5x B27 without vitamin A, 0.3% glucose, 20 ng/ml BDNF (Peprotech), 20 ng/ml GDNF (Peprotech), 500 ng/ml cAMP (Millipore-Sigma), 200 uM ascorbic acid (Millipore-Sigma)), supplemented with 0.2 uM Compound E. Post-mitotic neurons were maintained in NDM, with half media changes performed twice weekly. All drug treatments were performed by adding NDM containing candidate mitochondria compounds or vehicle 24 hours prior to collection, recording, or live cell assays. For mitochondria morphology experiments, neurons were infected with LV expressing MitoGFP

(LV-hSyn-mitoGFP) at 3 weeks of differentiation and analyzed one week later (4 weeks of differentiation). For shCNOT1 experiments, cells were infected with LV expressing shNC or shCNOT1 48 hours after plating for terminal differentiation, instead of at the NPC stage due to improve cell viability. For RACK1 rescue experiments, neurons were infected with LV -BFP or LV -RACK1-BFP virus at 3.5 weeks after plating to be consistent with the timing of leflunomide experiments.

See also Table S1. Cell lines and animal models used in this study.

Mouse husbandry and Isolation of mouse astrocytes—We performed all procedures involving live mice in accordance with the NIH Guide for the Care and Use of Laboratory Animals and the protocols approved by the University of Wisconsin-Madison Animal Care and Use Committee. The C57BL/6J mice (JAX stock #000664) were purchased from Jackson Laboratory and maintained in house. Mice were housed in groups and maintained on a 12-h light/dark cycle with food and water available ad libitum. Mouse astrocytes were isolated from the telencephalon of newborn wild-type C57BL/6J mice using a published protocol[7,22,67]. Briefly, P0-P3 mouse forebrain were dissected and digested with trypsin for 5 min, cells were then dissociated by harsh trituration to avoid growing of neurons and plated onto T25 flasks in DMEM supplemented with 10% FBS. The isolated cells were plated in T25 flasks and cultured in a 37°C, 5% CO2 incubator until cells reached confluence. The flasks were then shaken at 100 rotations/min for 2 days at 37°C to shake off proliferating cells and neurons. The media were changed. The cells were passaged a total of three times before the astrocytes were used for coculture experiment with human neurons.

METHOD DETAILS

Histological and neuronal morphology analysis of cultured fetal organotypic slices—Fetal organotypic brain slices were fixed in fixative (Sakura, Tissue-Tek VIP Fixative) for 24 hours. Organotypic slices were cryoprotected in sucrose 30%, embedded in OCT, and sectioned using cryostat at 40 μm. For immunostaining, tissue sections were pre-blocked with TBS++ (TBS containing 3% goat or donkey serum and 0.2% Triton X-100) for 1 h at room temperature, followed by incubation with primary antibodies diluted in TBS++ overnight in 4 °C. After washing 3 times, secondary antibodies were incubated 1 h at room temperature. All sections were counterstained with a nuclear counter stain, DAPI (4’, 6-diamidine-2’-phenylindole dihydrochloride, 1:2000, Roche Applied Science, Indianapolis, IN). After staining, autofluorescence eliminator reagent (Millipore, 2160) was used to reduce autofluorescence according to the manufacturer’s instructions. Sections were mounted and maintained at −20 °C in the dark until analysis. The signal intensity of nitrotyrosine of mCherry positive cells was quantified using Image J software as previously described[7,22]. The z-stack images (1 μm interval for intensity quantification, 0.1 um interval for mitochondrial morphology analysis) were acquired using a Nikon A1 confocal microscope. At least fifty mCherry positive cells were randomly selected from 2–3 cortical sections in each individual sample and the fluorescent intensity of nitrotyrosine was measured after subtracting background pixel intensity in the same image using Image J software (NIH). Mitochondrial morphological parameters including mitochondrial aspect ratio, area were analyzed using ImageJ (RRID:SCR_003070) with mitochondrial

morphology plug-in as previously described[7]. Approximately thirty neurons were analyzed for each group in each experiment. Samples from at least three individual biological samples were analyzed for experimental condition except as specified.

Whole cell recording of human fetal organotypic slices—Slices were transferred to a recording chamber (Warner Inc.), and whole-cell patch-clamp recordings of human neurons were performed as described[22,68]. Briefly, the recording was made using a Multipatch 700B amplifier, digitized with a Digidata 1440A, and acquired using pClamp 10 (Axon Instruments, Molecular Devices, CA). The extracellular solution contained (in mM): 119 NaCl, 5 KCl, 1.3 $MgCl_2$, 2 $CaCl_2$, 20 glucose, and 20 HEPES at pH = 7.4. Only neurons showing red fluorescence were picked for recording. Series resistance was typically within 10–30 MΩ. To evaluate the neuronal intrinsic excitability, currents were injected into neurons in current clamp mode. The resting membrane potential was measured, and the input resistance was calculated. The pipette solution for this experiment contained the following (in mM): 140 K-gluconate, 7.5 KCl, 10 HEPES-K, 0.5 EGTA-K, 4 Mg-ATP, and 0.3 Li-GTP, pH=7.2.

Measurement of mitochondrial membrane potential (MMP)—MMP analyses were performed as described with minor modifications[7]. Briefly, NPCs were plated onto poly-o/laminin-coated 96 well imaging plates (CellVis, P96–1.5P; 25,000 cells per well) using the procedures described above. The mitochondrial membrane potential in human neurons was determined by JC-10 Mitochondrial Membrane Potential Assay Kit (Abcam), following the manufacturer's protocol. Briefly, neurons were stained with 1x JC-10 dye in Buffer A solution added directly to NDM for 30 min at 37 °C. After adding Buffer B, neurons were imaged using either the Operetta (Perkin-Elmer) or Nano (Molecular Devices) high content imaging system with a 20x objective (96 well plates) in 20% oxygen and 5% CO_2 at 37°C. For each well, a tile of 16 (Nano) or 20 (Operetta) individual fields were imaged Cells were also incubated with NucBlue Live Cell Stain (Life Technologies) or SYTO™ Deep Red (for shRNA experiments) nuclear stain, which was added to Buffer A prior to incubation. The mitochondrial membrane potential was assessed by quantifying the ratio of the intensity of red fluorescence (emission wavelength 590 nm) to green fluorescence (emission wavelength 520 nm) using Columbus (Perkin-Elmer) or MetaXpress (Molecular Devices) by establishing pipelines for batch analysis of images. Briefly, device-specific software was used to establish a mask of the nucleus and cell body based on nuclear dye and green JC10 channel, then this mask was used by the software for fluorescence intensity quantification. Pipelines were established to eliminate dead cells or occasional non-neuronal cells based on nucleus intensity and size, and to eliminate border objects from analysis. All images were also manually checked to exclude any images that were unusable (out of focus, large aggregates of cell bodies, presence of large debris). Only fields with similar cell density were compared to eliminate density as a potential confounding variable, which was achieved by establishing a cutoff for minimum and maximum number of total cells per image (100–300 identified objects). For drug treatments, cells were imaged 24 hours after addition of the compound or vehicle 4 weeks after plating for terminal differentiation.

See also Table S7, related to Figure 6. Assessment of mitochondrial protecting compounds.

Microelectrode array (MEA) analysis—MEA analyses of human neurons were performed as described[22]. Briefly, NPCs were seeded onto poly-o/laminin-coated 96 well Cytoview MEA plates (Axion Biosystems) at a density of 50,000 cells per well using the procedures described above. One week after plating, 10,000 primary mouse astrocytes resuspended in NDM + 10% FBS were added per well of the MEA plate. FBS was removed 48 hours later by replacing medium with standard NDM. MEA recordings occurred starting one week after the addition of astrocytes and were performed weekly, on the same day and always at a minimum of 24 hours after media changes. Half NDM changes were performed twice weekly. Extracellular recordings were performed in a Maestro Pro MEA system preset at 37°C and 5% CO_2 equipped with AxIS Navigator software (Axion Biosystems) using a bandwidth filter for 200 Hz to 3 kHz cutoff frequencies. Each plate was acclimatized for 5 min in the Maestro Instrument and recorded for 15 min for quantification. Spike detection was performed using an adaptive threshold set to 6 times the standard deviation of the estimated noise on each electrode. MEA analysis was performed using the Axion Biosystems Neural Metrics Tool and Metric Plotting Tool. An electrode was considered active at a threshold of 5 spikes/min. Sample sizes for each treatment are indicated in figure legends or in Table S1. Wells with < 25% active electrodes were not included in the data analysis. Single-electrode and network bursts were determined using the default parameters in AxIS Navigator. Single-electrode bursts were defined as a minimum of 5 spikes and a maximum interspike interval (ISI) of 100 ms. Network bursts were defined as a minimum of 50 spikes, maximum ISI of 100 ms, and minimum of 35% participating electrodes. Mean firing rate was estimated with a 10s detection window. Synchrony was calculated using a 20 ms window size. For drug treatments, cells were recorded for 15 minutes to establish baseline, then candidate mitochondria compound or vehicle diluted in NDM was added to the MEA plate. Cells were recorded 24 hours after addition of the compound for 15 minutes, then immediately had media replaced to stop drug treatment. Drug treatments were performed 3, 4, and 5 weeks after the addition of astrocytes.

See also Table S2. Related to Figure 2. MEA analysis of neurons.

See also Table S4. Related to Figure 4 and Figure S5. Effect of knocking down FMRP targets on MEA.

Immunocytochemistry and morphology analysis of cultured human neurons—Immunocytochemical analysis of cultured human neurons were carried as described[22,24]. Neurons cultured on coated glass coverslips or glass 8-well chamber slides (Nunc Lab-Tek II, Thermo Fisher Scientific; 200,000 cells per well) were fixed with 4% PFA for 15 minutes at room temperature and then washed twice with PBS. Neurons were blocked with TBS++ (TBS containing 3% goat or donkey serum and 0.2% Triton X-100) for 1 h at room temperature. Primary antibodies were diluted in TBS++ and incubated overnight at 4 °C. Samples were washed three times with TBS and incubated with Alexa Fluor-conjugated secondary antibodies (Thermo Fisher Scientific) diluted in TBS++ for 60 minutes at room temperature. After 3 washes with PBS, neurons were counterstained with a nuclear counter stain, DAPI (4’, 6-diamidine-2’-phenylindole dihydrochloride, 1:2000, Roche Applied Science, Indianapolis, IN) and coverslipped in DAVCO-PVA. The z-stack images with 0.1 um interval were acquired using a 60X oil objective on a Nikon A1 confocal

microscope. The Morphology of mitochondria in proximal neurites was analyzed using ImageJ (RRID: SCR_003070) with mitochondrial morphology plug-in. 3D reconstruction of mitochondria was performed using Bitplane IMARIS 8.0.3D image analysis software (Oxford Instruments, Concord, MA). Samples from at least three individual differentiations were analyzed for experimental condition for human neurons.

CLIP-seq and analysis—The CLIP-seq was carried out as described[24]. This procedure was modified from eCLIP[69]. Briefly, FMRP-FLAG (H1-FLAG, H13-FLAG, GM1-FLAG) and isogenic control (H1, H13, GM1) hPSCs were differentiated into neurons using dual SMAD method. 1 week after neuronal differentiation, mouse forebrain primary astrocytes were added to neurons. At 8-week of differentiation, neurons were crosslinked with 254-nm UV-C followed by cell lysis and partial digestion of RNAs. FMR1-bound RNAs were isolated by immunoprecipitation, dephosphorylated, and ligated to a dye-labeled 3′ adapter. Samples were then resolved using SDS-PAGE and transferred to nitrocellulose membranes. FMR1-bound RNAs were visualized and size selected by cutting the membranes. Size-selected RNAs were purified by Proteinase K digestion and ethanol precipitation. The purified RNAs from IP and size-matched input were converted to cDNAs followed by circularization of the cDNAs. cDNA libraries were constructed from the cDNAs by PCR amplification, and libraries were sequenced using Illumina HiSeq 2500.

The demultiplexed FASTQ files were first quality filtered using fastq_quality_filter of FASTX Toolkit (v0.0.14) with parameters “-q25 -p80”. Adapter sequences were then removed from reads using cutadapt (v1.7.1) with parameters “-n 3 -e 0.1 -O 5 -q 6 -m 20 -a AGATCGGAAGAGCACACG”. PCR duplicates were removed using fastx_collapser of FASTX Toolkit. Finally 5’ adapter sequences were trimmed from reads using fastx_trimmer of FASTX Toolkit with parameters “-f 13 -l 94”. Processed reads were mapped to the genome indices (generated by STAR from sequence file, GRCh38.primary_assembly.genome.fa, and annotation file, gencode.v27.chr_patch_hapl_scaff.basic.annotation.gtf, from GENCODE Release 27) using STAR (v2.5.3a) with parameters “STAR --runMode alignReads --runThreadN 8 --genomeLoad LoadAndKeep --genomeDir $genome --readFilesIn $file --outSAMunmapped None --outFilterMultimapNmax 1 --outFilterMultimapScoreRange 1 --outFilterMismatchNmax 2 --outFilterMismatchNoverLmax 0.1 --alignIntronMin 20 --alignIntronMax 1000000 -alignSJDBoverhangMin 1 --outFilterIntronMotifs RemoveNoncanonicalUnannotated --outSAMtype SAM --quantMode GeneCounts --outFileNamePrefix $file_ --outSAMattributes All --outFilterType BySJout --outSAMattrRGline ID:foo --alignEndsType EndToEnd”. Number of reads uniquely mapped to each gene were counted by STAR using the above parameter “--quantMode GeneCounts”. Only reads mapped to the forward strand were counted. The CLIP-seq data were analyzed using CLIPper[69]. CLIPper pipeline was adapted from the ENCODE eCLIP-seq processing pipeline v2.0. The peaks with fold change > 2 and p values <0.05 were used to define CLIPper lists of FMR1 target genes and 36 genes were identified for further validation.

See also Table S3, related to Figure 3. FMRP CLIP target and Gene set enrichment analyses

Co-Immunoprecipitation Mass Spectroscopy and analysis (Co-IP-MS)—Co-IP was performed followed by LC-MS. Briefly, H1-FMR1-FLAG hESCs were differentiated into neurons using dual SMAD method. At 4 weeks of differentiation, neurons were crosslinked with 0.1 mM DSS in phosphate-buffered saline (20mM sodium phosphate, 150mM NaCl, pH8.0) for 30 minutes at room temperature. Crosslinking was stopped by adding Tris solution (final concentration of 20mM Tris) and incubating for 15 minutes at room temperature, followed by cell lysis in RIPA buffer (50 mM Tris, 150 mM NaCl, 5 mM EDTA, 0.1% SDS, 0.5% sodium deoxycholate, 1% Tween 20, pH 7.5). A replicate experiment without crosslinking reagent DSS was included as comparison. A monoclonal antibody against FLAG was first coupled with Dynabeads using the Dynabeads® Antibody Coupling Kit (Life technologies) following the manufacturer's protocol. The antibody-coupled beads were then incubated with total protein lysate at 4 °C for 2 hours. After the fourth stringent wash with RIPA buffer, the immunoprecipitations were eluted with the Elution buffer (60 mM Glycine-HCl, 0.5% (w/v) SDS, pH 2.0). A quarter of the elution samples were subjected to silver staining to check the co-IP quality and the rest was subjected to mass spectrometry analysis conducted by the Mass Spectrometry Facility in UW-Madison Biotechnology Center. FMRP interactors were selected based on enrichment ratio (DSS crosslinked vs non-crosslinked) ≥ 1.2.

See also Table S5, related to Figure 5. FMRP interactors identified using co-IP.

See also Table S6, related to Figure 5. FMRP_CLIP_CoIP-trajectory overlap.

Bioinformatics analysis—Enrichment analysis was performed on the lists of CLIP-seq genes and FMRP_coIP genes individually using Metascape (https://metascape.org/gp/index.html#/main/step1) and gProfiler (https://biit.cs.ut.ee/gprofiler/gost). Metascape performed pathway and process enrichment analysis using ontology data resources including: KEGG Pathway, GO Biological Processes, Reactome Gene Sets, Canonical Pathways, CORUM, WikiPathways and PANTHER Pathway. A hypergeometric test was performed using all of the genes in the background and the default settings were applied for Metascape to select enrichment terms (p-value < 0.01, minimum count of 3, enrichment factor > 1.5); the enrichment factor is the ratio between the observed counts and the counts expected by chance. In addition, Metascape provided enrichments from data resource ontologies like Transcription Factor Targets, DisGeNET, Cell Type Signatures, COVID. The gProfiler data resource utilized Gene Ontology data resources (GO Molecular Function, GO Cellular Component, GO Biological Process), biological pathways (KEGG, Reactome, and WikiPathways), regulatory motifs in DNA (TRANSFAC, miRTarBase), protein databases (Human Protein Atlas and CORUM), and human phenotype ontology (HP). The statistical domain scope only included the annotated genes and the significance threshold was the g:SCS (Set Counts and Sizes) threshold.

Correlation Analysis was performed using Medial Frontal Cortex (MFC) Reads per kilobase of transcript per Million reads mapped (RPKM) counts data from development PsychENCODE (BrainSpan) for developmental periods 2 to 7 (early fetal to late fetal development)[19]. Pairwise Pearson correlation (r) between the list of CLIP-seq genes with FMRP-coIP genes was calculated to construct a correlation matrix to relate genes

with one another based on their expression dynamic patterns across the human samples. ComplexHeatmap - Bioconductor package in R was used to construct heatmaps and perform agglomerative hierarchical clustering. We used the dendrogram provided from the clustering to group FMRP_coIP genes together and CLIP-seq genes together based on their correlations. The gene set overlaps were calculated by UpsetR package[70].

Comparison of FMRP targets and interactors with human developmental and disease risk-associated genes—Gene set enrichment analyses were run using two-sided Fisher's exact tests to compare FMRP CLIP targets and Co-IP interactors to sets of genes associated with ASD and NDD risk, to genes defined by their direction of expression change across human cortical development, and to genes with strong sequence constraint in the human population. Enrichment P-values were adjusted using Bonferroni correction for the number of tests performed within each of the following comparisons: CLIP targets versus ASD and NDD risk genes identified by exome sequencing[32,33,35] (6 tests), CLIP targets versus 6 co-expression modules with significantly differential expression in ASD and control cortex[36] (6 tests), CLIP targets and CoIP interactors versus genes with falling, non-transitional, and rising expression profiles in developing human cortex[25](6 tests), CLIP targets and CoIP interactors versus highly constrained genes[45] (pLI score ≥ 0.995; 2 tests). Background gene sets used for tests of ASD and NDD risk genes consisted of all protein-coding genes assessed for genetic variation by exome sequencing from each reference publication. Background gene sets used for co-expression modules and expression trajectories consisted of all genes meeting minimum expression level thresholds in the corresponding study. Background gene set used for test of constrained genes consisted of all genes with an estimated pLI score from Lek and colleagues[45]. We additionally compared FMRP targets as defined by studies of postnatal human[44] and mouse[37] tissue to genes with falling, non-transitional, and rising expression profiles in developing human cortex, using a background of all genes meeting minimum expression criteria in Werling et al[25], and correcting for 6 tests (2 data sets, 3 trajectories).

Production of lentivirus (LV)—LV production was performed as described previously[7,22,71] with modification. Briefly, lentiviral DNA was co-transfected with packaging plasmids pMDL, REV and pCMV-Vsvg into HEK293T cells using PEI method. The viral transfer vector DNA and packaging plasmid DNA were transfected into 5×15 cm dishes of cultured HEK293T cells using the PEI. The medium containing LV was collected at 48 and 72 hours post-transfection, pooled, filtered through a 0.2-μm filter, and concentrated using an ultracentrifuge at 19 k rpm for 2 hours at 4°C using a SW27 rotor (Beckman). The virus was washed once and then resuspended in 100 μl PBS. We routinely obtained 1×10^9 infectious viral particles/ml for LV.

Western Blotting—Primary antibodies used in this study are listed in the antibody table below. Cells were lysed in RIPA buffer (50 mM Tris, pH 8.0, 150 mM NaCl, 1% NP-40, 0.1% SDS) supplemented with protease inhibitors (Roche Applied Science). After centrifugation for 10 min at 4°C, supernatants were quantified by Protein Assay Dye Reagent Concentrate (Bio-Rad). 20 μg of total proteins were resolved by SDS-PAGE, transferred to nitrocellulose membrane, blocked with 5% BSA, and probed with primary

antibodies. Secondary antibodies conjugated with near infrared fluorescent dyes (IRDye 800CW or IRDye 680LT, LI-COR) were used at dilution of 1:10,000 for visualizing protein bands with an Odyssey Imager (LI-COR). Quantification of intensity was performed using FIJI (Image J) software. At least three independent biological replicates or differentiations were used for each experiment (Table S1).

Proximity Ligation Assays (PLA)—PLA was performed as described[22]. Cultured human neurons differentiated from FMRP-FLAG PSCs with or without LEF treatment were assessed by PLA according to the Duolink PLA Fluorescence Protocol (Sigma-Aldrich). Briefly, Neurons grown on coverslips were fixed with 4% paraformaldehyde in PBS for 20 minutes at RT, washed with PBS (3 × 5 minutes), permeabilized with 0.2% Triton X-100 in PBS for 15 minutes and blocked with the Duolink® Blocking Solution for 60 minutes at RT. The cells were then incubated at 4°C overnight in Duolink® Antibody Diluent containing the following primary antibodies: rabbit anti-CNOT1 and mouse anti-FLAG. After washes in 1x Wash Buffer A (Sigma-Aldrich, DUO82049), neurons were incubated with two PLA probes (Duolink In Situ PLA Probe Anti-Rabbit PLUS DUO92002 and Anti-Mouse MINUS DUO92004, Sigma-Aldrich) in Duolink® Antibody Diluent for 1 hour at 37°C, followed by washes with 1x Wash Buffer A and incubation in ligation solution (Duolink In Situ Detection Reagents Red, Sigma-Aldrich Duo92008) for 30 minutes at 37°C. Neurons were then washed with Wash Buffer A and incubated in the amplification solution (Sigma-Aldrich) for 100 minutes at 37°C to fluorescently label the ligated PLA probes. After amplification, neurons were further incubated with primary antibody against MAP2 for 60 minutes at RT, washed in PBST and incubated with secondary antibody for 60 minutes at RT. Neurons were then washed in PBS (3 × 5 minutes), stained with DAPI and rinsed in Wash Buffer B and 0.01x Wash Buffer B (Sigma-Aldrich, DUO82049). Microscopic imaging (60X) was done with a Nikon A1 confocal microscope.

RNA immunoprecipitation followed by quantitative PCR (RNA IP-qPCR)—RNA-IP followed by qPCR was performed as described previously[7,22,24,72]. Briefly, human fetal cortical tissues were Dounce homogenized in 2 ml of homogenization buffer (25 mM Tris (pH 7.0), 25 mM Tris (pH 8.0), 100 mM KCl, 12 mM MgCl2, 10% IGEPAL, 1 mM DTT, protease inhibitors, 1× RNase inhibitor, 200 units/mL, 100 μg/mL cycloheximide, 1 mg/mL heparin). 293 cells infected with LV-shRNAs were harvested and homogenized in the same buffer. Nuclei and debris were pelleted at 14,000 g for 15 min. An aliquot of input was saved for RNA extraction (50 μl). A polyclonal antibody against FMRP or CNOT1 was incubated with supernatant at 4 °C for 4 h before adding Dynabeads (Life Technologies). The antibody–protein conjugation was rotated at 4 °C overnight. After the third wash with the high-salt buffer (25 mM Tris (pH 7.0), 25 mM Tris (pH 8.0), 300 mM KCl, 12 mM MgCl2, 1 mM DTT, 100 μg/mL cycloheximide), the immunoprecipitations were resuspended into Trizol (Invitrogen) for RNA isolation. RNA from immunoprecipitation and input was used, and all qPCR reactions were carried out in duplicate for each sample on each amplicon.

Co-Immunoprecipitation Western Blot analysis (Co-IP-WB)—Co-IP was performed as described above (in Co-IP-MS). However the samples were analyzed by

western blotting as described[73]. Briefly, hPSCs were differentiated into neurons using dual SMAD method. HEK293 cells were transfected with FLAG-FMRP or FLAG-GFP. At 4 weeks of differentiation or 3 days after transfection, cells were crosslinked with 0.1 mM DSS in phosphate-buffered saline (20mM sodium phosphate, 150mM NaCl, pH8.0) for 30 minutes at room temperature. Crosslinking was stopped by adding Tris solution (final concentration of 20mM Tris) and incubating for 15 minutes at room temperature, followed by cell lysis in Lysis buffer (25 mM Tris, 150 mM NaCl, 1 mM EDTA, 5% Glycerol, 1% IGEPAL, pH 7.5). A replicate experiment without crosslinking reagent DSS was included as comparison. A polyclonal antibody against FMRP was incubated with total neuron protein lysate; a monoclonal antibody against FLAG was incubated with total HEK293 cell protein lysate. The antibody-protein lysate incubation was done at 4 °C for 4 hours before adding Dynabeads. Then, the antibody–protein conjugation was rotated at 4 °C overnight. After the fourth stringent wash with Wash buffer (25 mM Tris, 150 mM NaCl, 1 mM EDTA, 1% IGEPAL, pH 7.5), the immunoprecipitations were mixed with 2X SDS loading buffer and were subjected to Western Blot.

Real-Time quantitative PCR (qPCR)—Cells were collected in TRIzol reagent (Thermo Fisher Scientific) and stored at −80°C for all RNA expression experiments. Real-time PCR assays were performed using standard methods as previously described[22 7,71]. The first-strand cDNA was generated by reverse transcription with both oligo dT primer and random primers using PrimeScript™ RT Reagent Kit (Takara, #RR037A). To quantify the mRNA levels using real-time PCR, aliquots of first-strand cDNA were amplified with gene-specific primers and universal SYBR Green PCR supermix (Bio-Rad, #172–5124) using a Step-1 Real-Time PCR System (Applied Biosystems). The PCR reactions contained 20–40 ng of cDNA and 300 nM of forward and reverse primers in a final reaction volume of 20 μl.

See also Table S7, related to Figure 6. Assessment of mitochondrial protecting compounds.

mRNA stability assay—HEK293 cells were treated with 10 μg/ml of actinomycin D (Sigma-Aldrich) to inhibit gene transcription as described[7] and neurons were collected at various time intervals for RNA isolation and qPCR analysis. *RACK1* mRNA levels were normalized to *GAPHD*. RNA decay kinetics and half-life were analyzed using a published method[7]. Briefly, we used exponential function $M = M_0 e^{-\lambda t}$ (M: amount of mRNA at t time, M0: amount of mRNA t t=). $\lambda = (\ln)/T1/2$ (T1/2 is the half-life of the mRNA).

ATP levels using Cell Titer GLO—ATP levels in cultured hPSC-derived neurons were measured used CellTiter-Glo 2.0 reagent (Promega) according to the manufacturer's protocol. NPCs were plated for terminal differentiation onto 96 well white opaque flat bottom tissue cultured plates at a density of 25,000 cells per well. Four weeks after plating, neurons were treated with vehicle (0.1% DMSO) or 2 μM FCCP (Abcam), then placed at room temperature to equilibrate for 30 minutes as indicated in the protocol. A volume of Cell Titer GLO equal to the volume of culture medium present in each well was added (100 μl). The plate was mixed on a shaker for 2 minutes at room temperature to lyse cells, incubated at room temperature for 10 minutes, then the luminescence recorded using the preprogrammed CellTiter-GLO settings on a GloMax plate reader (Promega).

NAD and NADH levels using NAD GLO—Total levels of NAD+ and NADH in cultured hPSC-derived neurons was measured 4 weeks after plating using the NAD/NADH-Glo assay (Promega) according to the manufacturer's protocol. NPCs were plated for terminal differentiation onto 96 well white opaque flat bottom tissue cultured plates at a density of 25,000 cells per well. NAD/NADH-Glo Detection Reagent was prepared just prior to use for each assay, consisting of Luciferin Detection Reagent, Reductase, Reductase Substrate, NAD Cycling Enzyme, and NAD Cycling Substrate. Neurons were treated with vehicle (0.1% DMSO) or 2 μM FCCP for 30 minutes prior to performing assay. Cells were placed at room temperature for 5 minutes to equilibrate, then a volume of NAD/NADH-Glo Detection Reagent equal to the volume of culture medium present in each well was added (75 μl). The plate was mixed on a shaker for 2 minutes at room temperature to lyse cells, incubated for 40 minutes at room temperature, then luminescence recorded using a GloMax plate reader using an integration time of 0.5 seconds per well.

QUANTIFICATION AND STATISTICAL ANALYSIS

Data collection timing and blinding—Data collection was carried out for a predetermined period of time, as dictated by literature or core facility-based standards. All cell counting, tracing, quantification and behavioral analyses were performed by experimenters who were blind to the identity and treatments of the samples.

Statistical Analysis—Power analysis was used to pre-determine sample sizes, and our sample sizes are similar to those reported in previous publications (see citations within each procedure). Data distribution was assumed to be normal but this was not formally tested. Statistical analysis was performed using ANOVA and Student's *t* test, unless specified, with the aid of SPSS version 28 and GraphPad Prism 9. Unpaired or paired two-tailed Student *t* test for two-group comparisons, or two-tailed Welch's t-test of normalized data to account for unequal variances. Ordinary One-Way ANOVA was used for analysis of multiple experimental treatment compared to one control condition. Two-way ANOVA with Bonferroni post hoc test was used for analyzing multiple groups. Two-way repeated measures ANOVA with Sidak's multiple comparison test was used for analyzing MEA time course data. Outliers were identified using GraphPad Prism 9 software with ROUT method (Q=1%). Probabilities of $p < 0.05$ were considered as significant.

Schematics drawings were created using Power Point, Adobe Illustrator, Biorender, adaptation from a publication[64].

Supplementary Material

Refer to Web version on PubMed Central for supplementary material.

ACKNOWLEDGEMENTS

We thank Y. Xing, Y. Bao, K. Schoeller, R.D. Risgaard, M. Syed, and J. Le for technical assistance; K. Knobel at the Waisman IDD Model Core for services; Y. Yin and C. Soref, for generation of iPSCs; Dr. H. Simmons for non-human primate tissue acquisition. This work was supported by grants from the National Institutes of Health (R01MH118827, R01NS105200, and R01MH116582 to X.Z., a diversity supplement to R01MH118827 for S.O.S.; R01HD064743 to Q.C., R01NS064025, R01AG067025, and U01MH116492 to D.W., P51 OD011106 to the WNPRC, U54HD090256 and P50HD105353 to the Waisman Center, R24HD000836 to I.A.G), DOD

IIRA grant W81XWH-22-1-0621 (to X.Z. and A.B.), Brain Research Foundation, UW Vilas Mid-Career Award, Kellett Mid-Career Award, Wisconsin Alumni Research Foundation, and Jenni and Kyle Professorship (to X.Z.), Simons Foundation Autism Research Initiative pilot grant (to X.Z. Q.C., A.M.M.S., and D. W.) NARSAD Young Investigator Grant from the Brain and Behavior Research Foundation (28721 to A.M.M.S., 29815 to D.M.W.), Simons Foundation Autism Research Initiative Bridge to Independence Award 606289 (to D.M.W.), SciMed scholarships (to N.M.M-A and S.O.S.), T32 GM141013 Molecular Pharmacology training grant (to N.M.M-A), FRAXA Postdoctoral fellowships (to M.S. and C.L.S.), and postdoctoral fellowships from UW SCRMC and Autism Science Foundation (to C.L.S.).

INCLUSION AND DIVERSITY

We support inclusive, diverse, and equitable conduct of research.

REFERENCES

1. Hollis F, Kanellopoulos AK, and Bagni C (2017). Mitochondrial dysfunction in Autism Spectrum Disorder: clinical features and perspectives. Curr Opin Neurobiol 45, 178–187. 10.1016/j.conb.2017.05.018. [PubMed: 28628841]
2. Pei L, and Wallace DC (2018). Mitochondrial Etiology of Neuropsychiatric Disorders. Biol Psychiatry 83, 722–730. 10.1016/j.biopsych.2017.11.018. [PubMed: 29290371]
3. Kim Y, Vadodaria KC, Lenkei Z, Kato T, Gage FH, Marchetto MC, and Santos R (2019). Mitochondria, Metabolism, and Redox Mechanisms in Psychiatric Disorders. Antioxid Redox Signal 31, 275–317. 10.1089/ars.2018.7606. [PubMed: 30585734]
4. Pieretti M, Zhang FP, Fu YH, Warren ST, Oostra BA, Caskey CT, and Nelson DL (1991). Absence of expression of the FMR-1 gene in fragile X syndrome. Cell 66, 817–822. [PubMed: 1878973]
5. Verkerk AJ, Pieretti M, Sutcliffe JS, Fu YH, Kuhl DP, Pizzuti A, Reiner O, Richards S, Victoria MF, and Zhang FP (1991). Identification of a gene (FMR-1) containing a CGG repeat coincident with a breakpoint cluster region exhibiting length variation in fragile X syndrome. Cell 65, 905–914. [PubMed: 1710175]
6. Lozano R, Azarang A, Wilaisakditipakorn T, and Hagerman RJ (2016). Fragile X syndrome: A review of clinical management. Intractable & Rare Diseases Research 5, 145–157. 10.5582/irdr.2016.01048. [PubMed: 27672537]
7. Shen M, Wang F, Li M, Sah N, Stockton ME, Tidei JJ, Gao Y, Korabelnikov T, Kannan S, Vevea JD, et al. (2019). Reduced mitochondrial fusion and Huntingtin levels contribute to impaired dendritic maturation and behavioral deficits in Fmr1-mutant mice. Nat Neurosci. 10.1038/s41593-019-0338-y.
8. Bulow P, Wenner PA, Faundez V, and Bassell GJ (2021). Mitochondrial Structure and Polarity in Dendrites and the Axon Initial Segment Are Regulated by Homeostatic Plasticity and Dysregulated in Fragile X Syndrome. Front Cell Dev Biol 9, 702020. 10.3389/fcell.2021.702020. [PubMed: 34350185]
9. Bulow P, Zlatic SA, Wenner PA, Bassell GJ, and Faundez V (2021). FMRP attenuates activity dependent modifications in the mitochondrial proteome. Mol Brain 14, 75. 10.1186/s13041-021-00783-w. [PubMed: 33931071]
10. D'Antoni S, de Bari L, Valenti D, Borro M, Bonaccorso CM, Simmaco M, Vacca RA, and Catania MV (2020). Aberrant mitochondrial bioenergetics in the cerebral cortex of the Fmr1 knockout mouse model of fragile X syndrome. Biol Chem 401, 497–503. 10.1515/hsz-2019-0221. [PubMed: 31702995]
11. Griffiths KK, Wang A, Wang L, Tracey M, Kleiner G, Quinzii CM, Sun L, Yang G, Perez-Zoghbi JF, Licznerski P, et al. (2020). Inefficient thermogenic mitochondrial respiration due to futile proton leak in a mouse model of fragile X syndrome. FASEB J 34, 7404–7426. 10.1096/fj.202000283RR. [PubMed: 32307754]
12. Licznerski P, Park HA, Rolyan H, Chen R, Mnatsakanyan N, Miranda P, Graham M, Wu J, Cruz-Reyes N, Mehta N, et al. (2020). ATP Synthase c-Subunit Leak Causes Aberrant Cellular Metabolism in Fragile X Syndrome. Cell 182, 1170–1185 e1179. 10.1016/j.cell.2020.07.008. [PubMed: 32795412]

13. Kuzniewska B, Cysewski D, Wasilewski M, Sakowska P, Milek J, Kulinski TM, Winiarski M, Kozielewicz P, Knapska E, Dadlez M, et al. (2020). Mitochondrial protein biogenesis in the synapse is supported by local translation. EMBO Rep 21, e48882. 10.15252/embr.201948882. [PubMed: 32558077]

14. Yamasue H, Aran A, and Berry-Kravis E (2019). Emerging pharmacological therapies in fragile X syndrome and autism. Curr Opin Neurol 32, 635–640. 10.1097/WCO.0000000000000703. [PubMed: 31045620]

15. Sousa AMM, Meyer KA, Santpere G, Gulden FO, and Sestan N (2017). Evolution of the Human Nervous System Function, Structure, and Development. Cell 170, 226–247. 10.1016/j.cell.2017.06.036. [PubMed: 28708995]

16. Zhao X, and Bhattacharyya A (2018). Human Models Are Needed for Studying Human Neurodevelopmental Disorders. Am J Hum Genet 103, 829–857. 10.1016/j.ajhg.2018.10.009. [PubMed: 30526865]

17. Richter JD, and Zhao X (2021). The molecular biology of FMRP: new insights into fragile X syndrome. Nat Rev Neurosci 22, 209–222. 10.1038/s41583-021-00432-0. [PubMed: 33608673]

18. Castren ML (2016). Cortical neurogenesis in fragile X syndrome. Front Biosci (Schol Ed) 8, 160–168. 10.2741/s455. [PubMed: 26709905]

19. Zhu Y, Sousa AMM, Gao T, Skarica M, Li M, Santpere G, Esteller-Cucala P, Juan D, Ferrandez-Peral L, Gulden FO, et al. (2018). Spatiotemporal transcriptomic divergence across human and macaque brain development. Science 362. 10.1126/science.aat8077.

20. Contractor A, Klyachko VA, and Portera-Cailliau C (2015). Altered Neuronal and Circuit Excitability in Fragile X Syndrome. Neuron 87, 699–715. 10.1016/j.neuron.2015.06.017. [PubMed: 26291156]

21. Pilaz LJ, Lennox AL, Rouanet JP, and Silver DL (2016). Dynamic mRNA Transport and Local Translation in Radial Glial Progenitors of the Developing Brain. Curr Biol 26, 3383–3392. 10.1016/j.cub.2016.10.040. [PubMed: 27916527]

22. Guo Y, Shen M, Dong Q, Mendez-Albelo NM, Huang SX, Sirois CL, Le J, Li M, Jarzembowski ED, Schoeller KA, et al. (2023). Elevated levels of FMRP-target MAP1B impair human and mouse neuronal development and mouse social behaviors via autophagy pathway. Nat Commun 14, 3801. 10.1038/s41467-023-39337-0. [PubMed: 37365192]

23. Liu B, Li Y, Stackpole EE, Novak A, Gao Y, Zhao Y, Zhao X, and Richter JD (2018). Regulatory discrimination of mRNAs by FMRP controls mouse adult neural stem cell differentiation. Proc Natl Acad Sci U S A 115, E11397–E11405. 10.1073/pnas.1809588115. [PubMed: 30373821]

24. Li M, Shin J, Risgaard RD, Parries MJ, Wang J, Chasman D, Liu S, Roy S, Bhattacharyya A, and Zhao X (2020). Identification of FMR1-regulated molecular networks in human neurodevelopment. Genome Res. 10.1101/gr.251405.119.

25. Werling DM, Pochareddy S, Choi J, An JY, Sheppard B, Peng M, Li Z, Dastmalchi C, Santpere G, Sousa AMM, et al. (2020). Whole-Genome and RNA Sequencing Reveal Variation and Transcriptomic Coordination in the Developing Human Prefrontal Cortex. Cell Rep 31, 107489. 10.1016/j.celrep.2020.03.053. [PubMed: 32268104]

26. Doers ME, Musser MT, Nichol R, Berndt ER, Baker M, Gomez TM, Zhang SC, Abbeduto L, and Bhattacharyya A (2014). iPSC-derived forebrain neurons from FXS individuals show defects in initial neurite outgrowth. Stem cells and development 23, 1777–1787. 10.1089/scd.2014.0030. [PubMed: 24654675]

27. Yin Y, Petersen AJ, Soref C, Richards WD, Ludwig T, Taapken S, Berndt E, Zhang SC, and Bhattacharyya A (2019). Generation of seven induced pluripotent stem cell lines from neonates of different ethnic backgrounds. Stem Cell Res 34, 101365. 10.1016/j.scr.2018.101365. [PubMed: 30605841]

28. Connolly NMC, Theurey P, Adam-Vizi V, Bazan NG, Bernardi P, Bolanos JP, Culmsee C, Dawson VL, Deshmukh M, Duchen MR, et al. (2018). Guidelines on experimental methods to assess mitochondrial dysfunction in cellular models of neurodegenerative diseases. Cell Death Differ 25, 542–572. 10.1038/s41418-017-0020-4. [PubMed: 29229998]

29. Liu XS, Wu H, Krzisch M, Wu X, Graef J, Muffat J, Hnisz D, Li CH, Yuan B, Xu C, et al. (2018). Rescue of Fragile X Syndrome Neurons by DNA Methylation Editing of the FMR1 Gene. Cell 172, 979–992 e976. 10.1016/j.cell.2018.01.012. [PubMed: 29456084]
30. Zhou Y, Zhou B, Pache L, Chang M, Khodabakhshi AH, Tanaseichuk O, Benner C, and Chanda SK (2019). Metascape provides a biologist-oriented resource for the analysis of systems-level datasets. Nat Commun 10, 1523. 10.1038/s41467-019-09234-6. [PubMed: 30944313]
31. Raudvere U, Kolberg L, Kuzmin I, Arak T, Adler P, Peterson H, and Vilo J (2019). g:Profiler: a web server for functional enrichment analysis and conversions of gene lists (2019 update). Nucleic Acids Res 47, W191–W198. 10.1093/nar/gkz369. [PubMed: 31066453]
32. Satterstrom FK, Kosmicki JA, Wang J, Breen MS, De Rubeis S, An JY, Peng M, Collins R, Grove J, Klei L, et al. (2020). Large-Scale Exome Sequencing Study Implicates Both Developmental and Functional Changes in the Neurobiology of Autism. Cell 180, 568–584 e523. 10.1016/j.cell.2019.12.036. [PubMed: 31981491]
33. Fu JM, Satterstrom FK, Peng M, Brand H, Collins RL, Dong S, Wamsley B, Klei L, Wang L, Hao SP, et al. (2022). Rare coding variation provides insight into the genetic architecture and phenotypic context of autism. Nat Genet 54, 1320–1331. 10.1038/s41588-022-01104-0. [PubMed: 35982160]
34. Deciphering Developmental Disorders, S. (2017). Prevalence and architecture of de novo mutations in developmental disorders. Nature 542, 433–438. 10.1038/nature21062. [PubMed: 28135719]
35. Zhou X, Feliciano P, Shu C, Wang T, Astrovskaya I, Hall JB, Obiajulu JU, Wright JR, Murali SC, Xu SX, et al. (2022). Integrating de novo and inherited variants in 42,607 autism cases identifies mutations in new moderate-risk genes. Nat Genet 54, 1305–1319. 10.1038/s41588-022-01148-2. [PubMed: 35982159]
36. Parikshak NN, Swarup V, Belgard TG, Irimia M, Ramaswami G, Gandal MJ, Hartl C, Leppa V, Ubieta LT, Huang J, et al. (2016). Genome-wide changes in lncRNA, splicing, and regional gene expression patterns in autism. Nature 540, 423–427. 10.1038/nature20612. [PubMed: 27919067]
37. Darnell JC, Van Driesche SJ, Zhang C, Hung KY, Mele A, Fraser CE, Stone EF, Chen C, Fak JJ, Chi SW, et al. (2011). FMRP Stalls Ribosomal Translocation on mRNAs Linked to Synaptic Function and Autism. Cell 146, 247–261. [PubMed: 21784246]
38. Maurin T, Lebrigand K, Castagnola S, Paquet A, Jarjat M, Popa A, Grossi M, Rage F, and Bardoni B (2018). HITS-CLIP in various brain areas reveals new targets and new modalities of RNA binding by fragile X mental retardation protein. Nucleic Acids Research, gky267–gky267. 10.1093/nar/gky267.
39. Sawicka K, Hale CR, Park CY, Fak JJ, Gresack JE, Van Driesche SJ, Kang JJ, Darnell JC, and Darnell RB (2019). FMRP has a cell-type-specific role in CA1 pyramidal neurons to regulate autism-related transcripts and circadian memory. Elife 8, e46919. 10.7554/eLife.46919. [PubMed: 31860442]
40. Masi M, Attanzio A, Racchi M, Wolozin B, Borella S, Biundo F, and Buoso E (2022). Proteostasis Deregulation in Neurodegeneration and Its Link with Stress Granules: Focus on the Scaffold and Ribosomal Protein RACK1. Cells 11. 10.3390/cells11162590.
41. Battaini F, Pascale A, Lucchi L, Pasinetti GM, and Govoni S (1999). Protein kinase C anchoring deficit in postmortem brains of Alzheimer's disease patients. Exp Neurol 159, 559–564. 10.1006/exnr.1999.7151. [PubMed: 10506528]
42. Yan Z, and Rein B (2021). Mechanisms of synaptic transmission dysregulation in the prefrontal cortex: pathophysiological implications. Mol Psychiatry. 10.1038/s41380-021-01092-3.
43. Willsey AJ, Sanders SJ, Li M, Dong S, Tebbenkamp AT, Muhle RA, Reilly SK, Lin L, Fertuzinhos S, Miller JA, et al. (2013). Coexpression networks implicate human midfetal deep cortical projection neurons in the pathogenesis of autism. Cell 155, 997–1007. 10.1016/j.cell.2013.10.020. [PubMed: 24267886]
44. Tran SS, Jun HI, Bahn JH, Azghadi A, Ramaswami G, Van Nostrand EL, Nguyen TB, Hsiao YE, Lee C, Pratt GA, et al. (2019). Widespread RNA editing dysregulation in brains from autistic individuals. Nat Neurosci 22, 25–36. 10.1038/s41593-018-0287-x. [PubMed: 30559470]

45. Lek M, Karczewski KJ, Minikel EV, Samocha KE, Banks E, Fennell T, O'Donnell-Luria AH, Ware JS, Hill AJ, Cummings BB, et al. (2016). Analysis of protein-coding genetic variation in 60,706 humans. Nature 536, 285–291. 10.1038/nature19057. [PubMed: 27535533]
46. Vissers L, Kalvakuri S, de Boer E, Geuer S, Oud M, van Outersterp I, Kwint M, Witmond M, Kersten S, Polla DL, et al. (2020). De Novo Variants in CNOT1, a Central Component of the CCR4-NOT Complex Involved in Gene Expression and RNA and Protein Stability, Cause Neurodevelopmental Delay. Am J Hum Genet 107, 164–172. 10.1016/j.ajhg.2020.05.017. [PubMed: 32553196]
47. Chalabi Hagkarim N, and Grand RJ (2020). The Regulatory Properties of the Ccr4-Not Complex. Cells 9. 10.3390/cells9112379.
48. Soderberg O, Gullberg M, Jarvius M, Ridderstrale K, Leuchowius KJ, Jarvius J, Wester K, Hydbring P, Bahram F, Larsson LG, and Landegren U (2006). Direct observation of individual endogenous protein complexes in situ by proximity ligation. Nat Methods 3, 995–1000. 10.1038/nmeth947. [PubMed: 17072308]
49. Fox RI, Herrmann ML, Frangou CG, Wahl GM, Morris RE, Strand V, and Kirschbaum BJ (1999). Mechanism of action for leflunomide in rheumatoid arthritis. Clin Immunol 93, 198–208. 10.1006/clim.1999.4777. [PubMed: 10600330]
50. Miret-Casals L, Sebastian D, Brea J, Rico-Leo EM, Palacin M, Fernandez-Salguero PM, Loza MI, Albericio F, and Zorzano A (2018). Identification of New Activators of Mitochondrial Fusion Reveals a Link between Mitochondrial Morphology and Pyrimidine Metabolism. Cell Chem Biol 25, 268–278 e264. 10.1016/j.chembiol.2017.12.001. [PubMed: 29290623]
51. Abudupataer M, Zhu S, Yan S, Xu K, Zhang J, Luo S, Ma W, Alam MF, Tang Y, Huang H, et al. (2021). Aorta smooth muscle-on-a-chip reveals impaired mitochondrial dynamics as a therapeutic target for aortic aneurysm in bicuspid aortic valve disease. Elife 10. 10.7554/eLife.69310.
52. Yu M, Nguyen ND, Huang Y, Lin D, Fujimoto TN, Molkentine JM, Deorukhkar A, Kang Y, San Lucas FA, Fernandes CJ, et al. (2019). Mitochondrial fusion exploits a therapeutic vulnerability of pancreatic cancer. JCI Insight 5. 10.1172/jci.insight.126915.
53. Cheng N, Rho JM, and Masino SA (2017). Metabolic Dysfunction Underlying Autism Spectrum Disorder and Potential Treatment Approaches. Front Mol Neurosci 10, 34. 10.3389/fnmol.2017.00034. [PubMed: 28270747]
54. Kwan KY, Lam MM, Johnson MB, Dube U, Shim S, Rasin MR, Sousa AM, Fertuzinhos S, Chen JG, Arellano JI, et al. (2012). Species-dependent posttranscriptional regulation of NOS1 by FMRP in the developing cerebral cortex. Cell 149, 899–911. 10.1016/j.cell.2012.02.060. [PubMed: 22579290]
55. Kang Y, Zhou Y, Li Y, Han Y, Xu J, Niu W, Li Z, Liu S, Feng H, Huang W, et al. (2021). A human forebrain organoid model of fragile X syndrome exhibits altered neurogenesis and highlights new treatment strategies. Nat Neurosci 24, 1377–1391. 10.1038/s41593-021-00913-6. [PubMed: 34413513]
56. Adams DR, Ron D, and Kiely PA (2011). RACK1, A multifaceted scaffolding protein: Structure and function. Cell Commun Signal 9, 22. 10.1186/1478-811X-9-22. [PubMed: 21978545]
57. Liao S, Xiao S, Chen H, Zhang M, Chen Z, Long Y, Gao L, He J, Ge Y, Yi W, et al. (2017). The receptor for activated protein kinase C promotes cell growth, invasion and migration in cervical cancer. Int J Oncol 51, 1497–1507. 10.3892/ijo.2017.4137. [PubMed: 29048616]
58. Vandenberg GG, Dawson NJ, Head A, Scott GR, and Scott AL (2021). Astrocyte-mediated disruption of ROS homeostasis in Fragile X mouse model. Neurochem Int 146, 105036. 10.1016/j.neuint.2021.105036. [PubMed: 33785420]
59. Vandenberg GG, Thotakura A, and Scott AL (2022). Mitochondrial bioenergetics of astrocytes in Fragile X syndrome: new perspectives on culture conditions and sex effects. Am J Physiol Cell Physiol 322, C125–C135. 10.1152/ajpcell.00130.2021. [PubMed: 34817267]
60. Cao Z, Hulsizer S, Cui Y, Pretto DL, Kim KH, Hagerman PJ, Tassone F, and Pessah IN (2013). Enhanced asynchronous Ca(2+) oscillations associated with impaired glutamate transport in cortical astrocytes expressing Fmr1 gene premutation expansion. J Biol Chem 288, 13831–13841. 10.1074/jbc.M112.441055. [PubMed: 23553633]

61. Weisz ED, Towheed A, Monyak RE, Toth MS, Wallace DC, and Jongens TA (2018). Loss of Drosophila FMRP leads to alterations in energy metabolism and mitochondrial function. Hum Mol Genet 27, 95–106. 10.1093/hmg/ddx387. [PubMed: 29106525]
62. Geng J, Khaket TP, Pan J, Li W, Zhang Y, Ping Y, Cobos Sillero MI, and Lu B (2023). Deregulation of ER-mitochondria contact formation and mitochondrial calcium homeostasis mediated by VDAC in fragile X syndrome. Dev Cell 58, 597–615 e510. 10.1016/j.devcel.2023.03.002. [PubMed: 37040696]
63. Rahman S, and Rahman T (2017). Unveiling some FDA-approved drugs as inhibitors of the store-operated Ca(2+) entry pathway. Sci Rep 7, 12881. 10.1038/s41598-017-13343-x. [PubMed: 29038464]
64. Onorati M, Li Z, Liu F, Sousa AMM, Nakagawa N, Li M, Dell'Anno MT, Gulden FO, Pochareddy S, Tebbenkamp ATN, et al. (2016). Zika Virus Disrupts Phospho-TBK1 Localization and Mitosis in Human Neuroepithelial Stem Cells and Radial Glia. Cell Rep 16, 2576–2592. 10.1016/j.celrep.2016.08.038. [PubMed: 27568284]
65. Li M, Zhao H, Ananiev GE, Musser M, Ness KH, Maglaque DL, Saha K, Bhattacharyya A, and Zhao X (2016). Establishment of reporter lines for detecting fragile X mental retardation (FMR1) gene reactivation in human neural cells. Stem cells (Dayton, Ohio). 10.1002/stem.2463.
66. Zhang SC, Wernig M, Duncan ID, Brustle O, and Thomson JA (2001). In vitro differentiation of transplantable neural precursors from human embryonic stem cells. Nat Biotechnol 19, 1129–1133. 10.1038/nbt1201-1129. [PubMed: 11731781]
67. Barkho BZ, Song H, Aimone JB, Smrt RD, Kuwabara T, Nakashima K, Gage FH, and Zhao X (2006). Identification of astrocyte-expressed factors that modulate neural stem/progenitor cell differentiation. Stem Cells Dev 15, 407–421. 10.1089/scd.2006.15.407. [PubMed: 16846377]
68. Dong Q, Liu Q, Li R, Wang A, Bu Q, Wang KH, and Chang Q (2018). Mechanism and consequence of abnormal calcium homeostasis in Rett syndrome astrocytes. Elife 7. 10.7554/eLife.33417.
69. Van Nostrand EL, Pratt GA, Shishkin AA, Gelboin-Burkhart C, Fang MY, Sundararaman B, Blue SM, Nguyen TB, Surka C, Elkins K, et al. (2016). Robust transcriptome-wide discovery of RNA-binding protein binding sites with enhanced CLIP (eCLIP). Nat Methods 13, 508–514. 10.1038/nmeth.3810. [PubMed: 27018577]
70. Conway JR, Lex A, and Gehlenborg N (2017). UpSetR: an R package for the visualization of intersecting sets and their properties. Bioinformatics 33, 2938–2940. 10.1093/bioinformatics/btx364. [PubMed: 28645171]
71. Gao Y, Shen M, Gonzalez JC, Dong Q, Kannan S, Hoang JT, Eisinger BE, Pandey J, Javadi S, Chang Q, et al. (2020). RGS6 Mediates Effects of Voluntary Running on Adult Hippocampal Neurogenesis. Cell Rep 32, 107997. 10.1016/j.celrep.2020.107997. [PubMed: 32755589]
72. Shen M, Guo Y, Dong Q, Gao Y, Stockton ME, Li M, Kannan S, Korabelnikov T, Schoeller KA, Sirois CL, et al. (2021). FXR1 regulation of parvalbumin interneurons in the prefrontal cortex is critical for schizophrenia-like behaviors. Mol Psychiatry 26, 6845–6867. 10.1038/s41380-021-01096-z. [PubMed: 33863995]
73. Li Y, Stockton ME, Eisinger BE, Zhao Y, Miller JL, Bhuiyan I, Gao Y, Wu Z, Peng J, and Zhao X (2018). Reducing histone acetylation rescues cognitive deficits in a mouse model of Fragile X syndrome. Nat Commun 9, 2494. 10.1038/s41467-018-04869-3. [PubMed: 29950602]

HIGHLIGHTS

- FMRP is critical for mitochondrial functions in developing human cortical neurons
- FMRP interacts and regulates essential genes during human prenatal development
- FMRP interacts with CNOT1 to regulate RACK1, a species-specific FMRP target
- Enhancing mitochondrial functions rescues hyperexcitability of FXS neurons

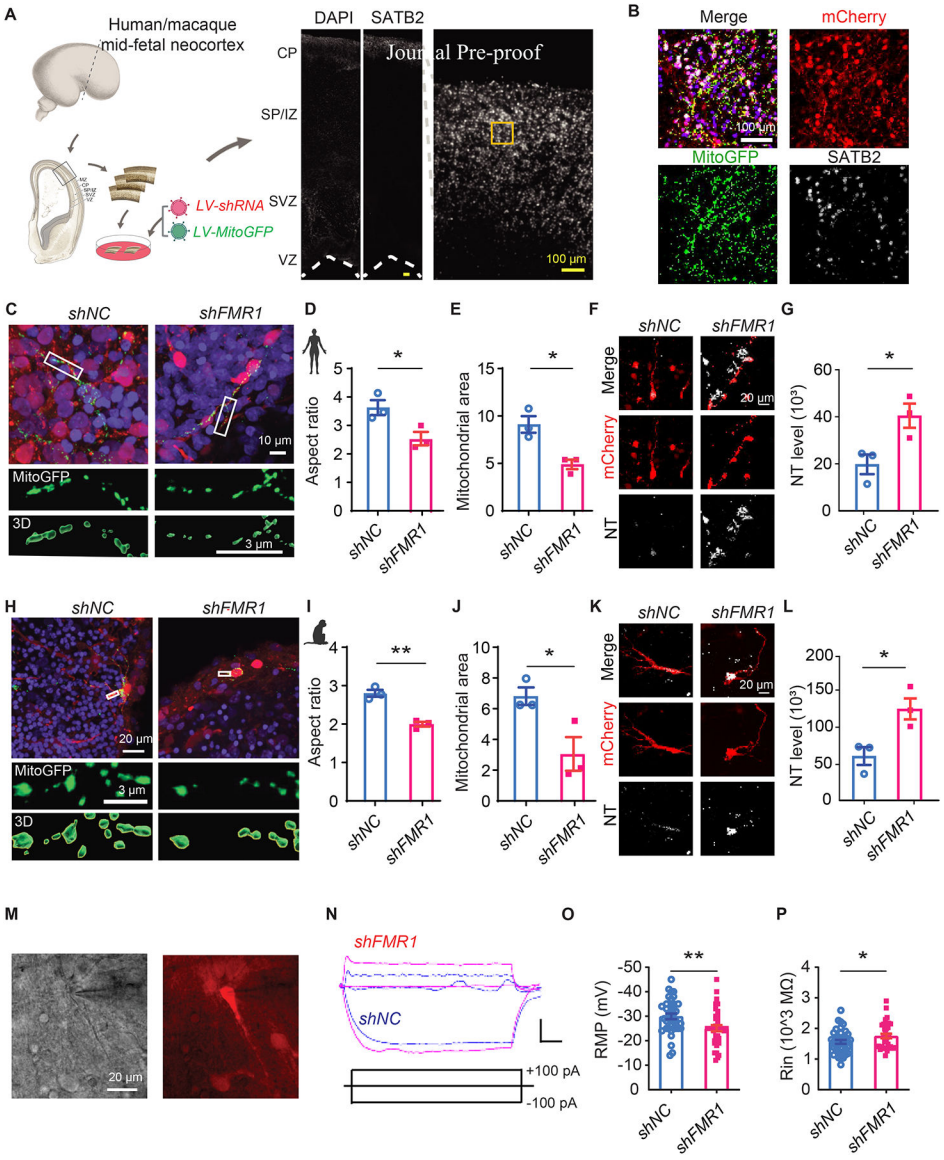

Figure 1. FMRP deficiency leads to mitochondrial deficits and hyperexcitability in primate cortical neurons in fetal neocortical organotypic slices.

(A-G) Mitochondrial analysis of FMRP-deficient (*shFMR1*) neurons in human and macaque mid-fetal cortical tissue compared to controls (*shNC*). (Schematics was adapted from[64])

(A) Experimental scheme for assessing mitochondria in neurons of *ex vivo* human cortical slices with FMRP knockdown using lentivirus (LV) expressing shRNA and mCherry (LV-*shFMR1*-mCherry). Immunostaining of human mid-fetal cortical tissue with neuronal marker (SATB2+) and nuclei (DAPI). Neurons in the cortical plate (yellow frame) were analyzed. VZ, ventricular zone; SVZ, subventricular zone; IZ, intermediate zone; SP, subplate; CP, cortical plate.

(B) Representative confocal images of LV-infected neurons (red), MitoGFP (green) and SATB2 (white).

(C, F) Representative confocal images of LV-infected neurons (red), MitoGFP (green) and NT (white).

(D, E, G) Quantification of mitochondrial aspect ratio (D), mitochondrial area (E) and NT levels (G).

(H-L) Mitochondrial analysis of FMRP-deficient neurons in macaque mid-fetal cortical tissue. Representative confocal images of LV-infected neurons (H, K) and quantification of mitochondrial aspect ratio (I), mitochondrial area (J) and NT levels (L).

(M-P) Whole-cell recording analysis of FMRP-deficient neurons on human mid-fetal cortex. (M) Representative images of a LV-infected mCherry+ neuron that has been patched.

(N) Example of potential trains upon current injections from LV-infected neurons. Scale bars showing amplitude (25 mV) and time (0.1 sec).

(O, P) Quantification of rest membrane potential (RMP, O) and input resistance (R_{in}, P). *shNC*: n = 38, *shFMR1*: n=36 cells from 3 biological replicates.

Two-tailed Student's test. Mean ± SEM from ⩾3 biological replicates. *p < 0.05, **p < 0.01. See also Figure S1.

See also Table S1 for detailed information on samples used

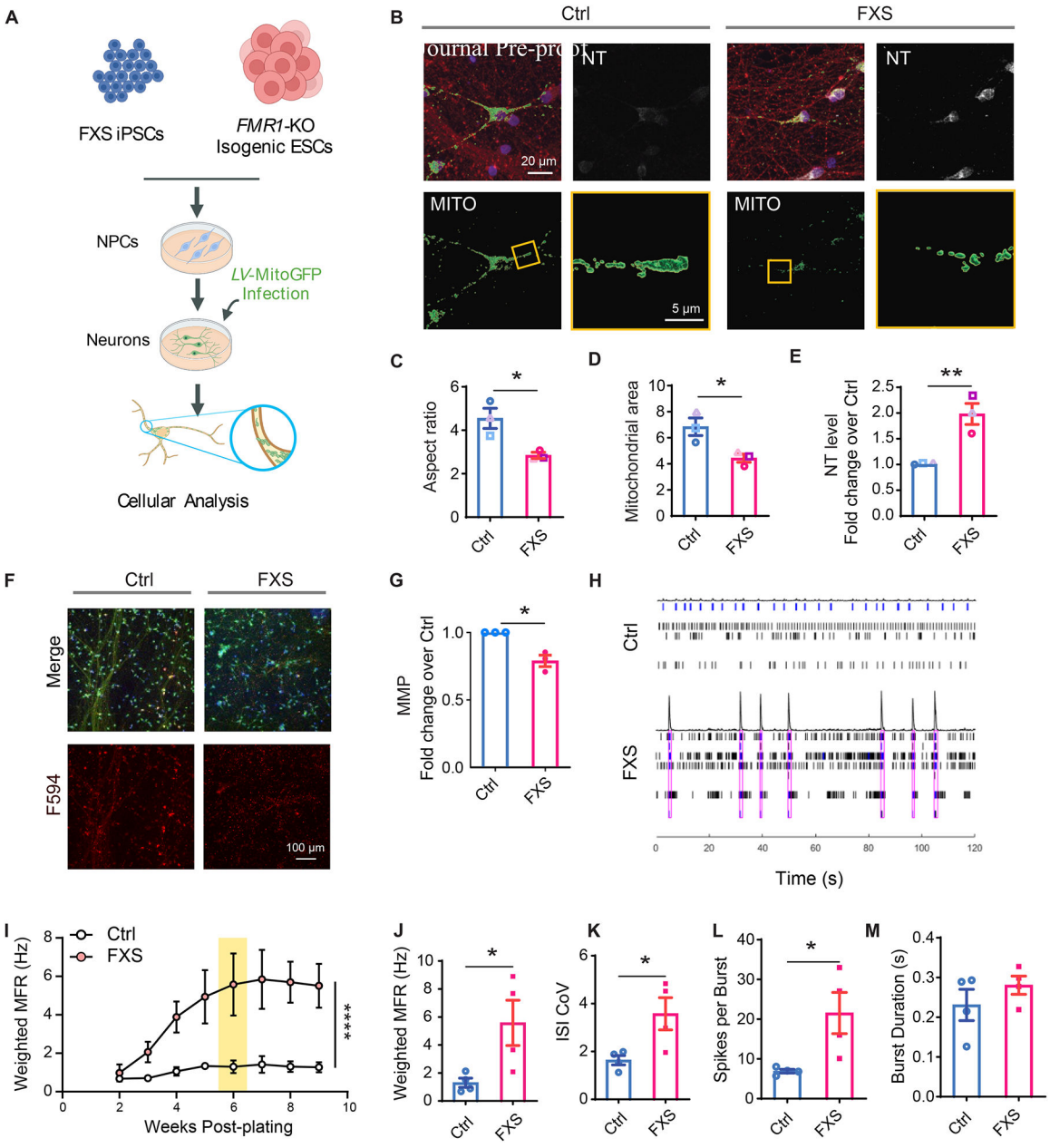

Figure 2. Human FXS neurons exhibit mitochondrial deficits and hyperexcitability

(A-G) Mitochondrial analyses of human FXS iPSC differentiated neurons (FXS) compared to control iPSC differentiated neurons (Ctrl). N=3 cell lines, 3 differentiations for each cell line.

(A) Experimental scheme for assessing mitochondria in neurons of human neurons.

(B) Representative confocal images of human neurons stained with Mito-GFP (MITO, green), TUJ1 (red), and nitrotyrosine (NT, white) and 3D reconstruction of mitochondria (yellow frame) at 4 weeks after differentiation.

(C-E) Quantification of mitochondrial aspect ratio (C), mitochondrial area (D), mitochondrial membrane potential (MMP, D) and NT level (E).

(F, G) Representative images (F) and quantification (G) of MMP of FXS neurons at 4 weeks after differentiation.

(H-M) Electrophysiological characterization of human FXS neurons using MEA.

(H) Representative raster plots showing 120 s of activity of FXS neurons and Ctrl neurons.

(I-M) Quantification of weighted MFR (I, J), ISI CoV (K), number of spikes per burst (L) and burst duration (M) of FXS neurons recorded starting at 2 to 9 weeks post-plating (I) and 6 weeks post-plating (J-M).

Two-tailed Student's test in (C-D, J-M). Two-tailed Student's test with Welch's correction in (E and G). Two-way ANOVA with Bonferroni post hoc test in (I). Mean ± SEM. C-E: N = 3; G and I-M, N = 1, n = 4. *$p < 0.05$, **$p < 0.01$, and ****$p < 0.0001$.

See also Figure S2. See also Table S1 for detailed information on cell lines used

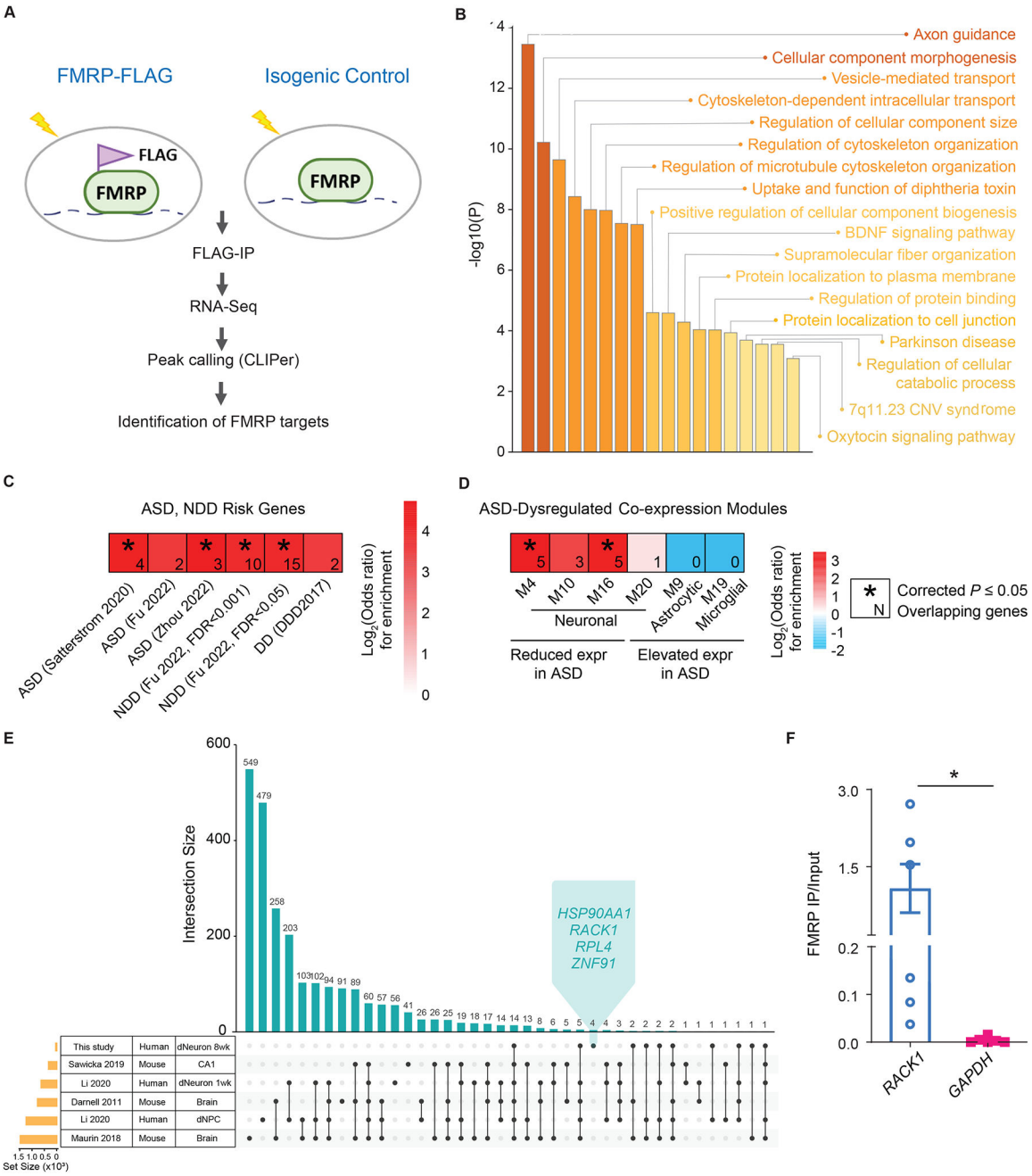

Figure 3. FMRP targets in human mature neurons

(A) Workflow of CLIP-seq. FMRP-FLAG neurons and their isogenic control neurons were subjected to UV crosslinking, immunoprecipitated using an anti-FLAG antibody followed by next generation sequencing (RNA-seq).

(B) Enrichments of GO biological processes of FMRP targets identified using CLIP-seq of mature human neurons. Y-axis: −log10(p value of enrichment).

(C) Gene set enrichment analyses (two-sided Fisher's exact test, FET) for CLIP target genes with published sets of ASD and NDD risk genes.

(D) Enrichment analyses (FET) for CLIP target genes with ASD-dysregulated co-expression modules in human cortex tissue.

(E) Overlaps of FMRP targets in human mature neurons (dNeuron_8wk) with previously identified FMRP targets in human NPCs (dNPCs)[24], human neurons (dNeuron_1wk)[24], juvenile mouse forebrains[37,38], and adult mouse hippocampal CA1[39]. Y-axis represents the intersection numbers of gene sets. See also Figure S4, S5.

(F) RNA immunoprecipitation followed by quantitative PCR (RNA-IP-qPCR) to detect binding of FMRP to *RACK1* mRNA in human mid-fetal cortical tissue. Two-tailed Student's test in (F). Mean ± SEM from ⩾3 independent experiments. p value, *p < 0.05.

See also Figure S3, S4. See also Table S1 for detailed information on cell lines used

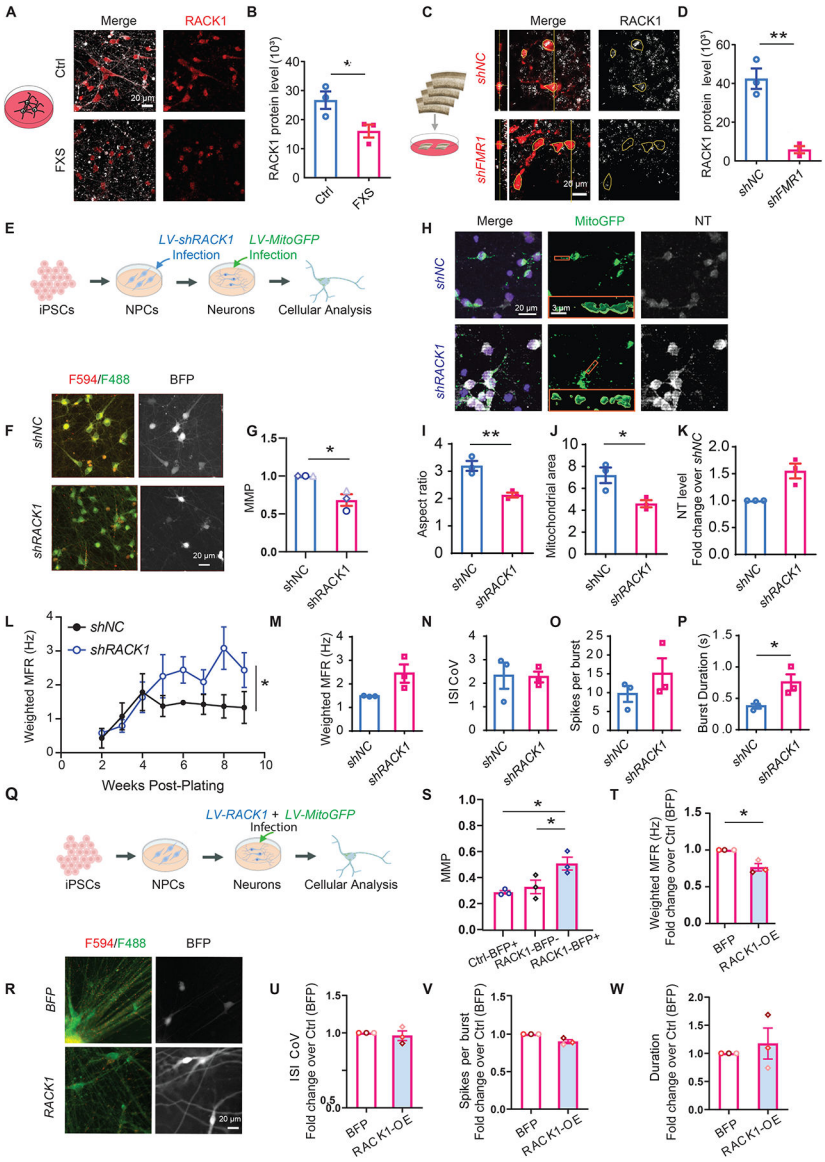

Figure 4. Reduced RACK1 expression in human neurons leads to mitochondrial deficits and hyperexcitability and overexpression of RACK1 rescues FXS neurons

(A-D) RACK1 protein expression levels in FXS neurons (A, B) and in FMRP-deficient neurons of human fetal cortical tissue (C, D), compared to controls. Schematics was adapted from[64]

(A) Representative confocal images of human neurons stained with RACK1 (red), TUJ1 (white) at 4 weeks after differentiation.

(B) Quantification of RACK1 protein expression levels.

(C) Representative confocal images of human cortical tissues stained with shRNA-mCherry (red) and RACK1 (white).

(D) Quantification of RACK1 protein expression levels.

(E-K) Mitochondrial analysis of LV-*shRACK1* infected neurons.

(E) Experimental scheme for assessing mitochondria in LV-*shRACK1* infected neurons.

(F, G) JC-10 assay of LV-*shRACK1* infected neurons.

(F) Representative images JC-10 dye-stained LV-*shRNA*-infected neurons at 4 weeks after differentiation.
(G) Quantification of the ratio of red (F594) and green (F488) fluorescence as MMP level of LV-*shRACK1, shCRMP1,shDYNC1H1, shSPTBN1* infected neurons. Each data point represents the average 594:488 ratio across 7–16 fields (>100 cells per field).
(H) Representative confocal images of LV-infected neurons expressing shRNA-BFP (blue), NT (white), MitoGFP (green) and 3D reconstruction of mitochondria.
(I-K) Quantification of mitochondrial aspect ratio (G), mitochondrial area (H) and NT level (I, $p = 0.0577$).
(L) Quantification of weighted mean firing rate (WMFR) of LV-*shRNA*-infected control neurons. N = 3 biologically independent cell lines (Ctrl, Ctrl-2, Ctrl-3).
(M-P) Quantification of weighted MFR (M), ISI CoV (N), number of spikes per burst (O) and burst duration (P) in the LV-*shRNA*-infected control neurons shown in (L) at the 6 week time point.
Two-tailed Student's test in (B, D, G-I, K, M-P). Two-way ANOVA with Bonferroni post hoc test in (L).
(Q-W) Overexpression of RACK1 in FXS neurons using LV (LV-*RACK1-BFP* or control LV-BFP) infection.
(Q): Experimental scheme for overexpressing RACK1 in FXS neurons
(R) Representative images JC-10 dye-stained LV-RACK1-BFP or control LV-BFP infected neurons at 4 weeks after differentiation.
(S) Quantification of the ratio of red (F594) and green (F488) fluorescence as MMP level in control LV-BFP infection neurons, and BFP+ neurons in LV-RACK1-BFP infected neurons and BFP- neurons in LV-RACK1-BFP infected neurons. Each data point represents the average 594:488 ratio across 5–15 fields (≥40 cells per data point). ONE-WAY ANOVA. n = 3 wells/technical replicates from 1 cell line
(T-W) MEA analysis: quantification of weighted mean firing rate (WMFR, T), ISI CoV (U), number of spikes per burst (V), and burst duration (W) in the LV-RACK1-BFP-infected control neurons compared to control LV- BFP-infected neurons at the 9-week time point. Mean ± SEM from ⩾3 biological replicates. *$p < 0.05$, and **$p < 0.01$.
See also Figure S5. See also Table S1 for detailed information on cell lines used

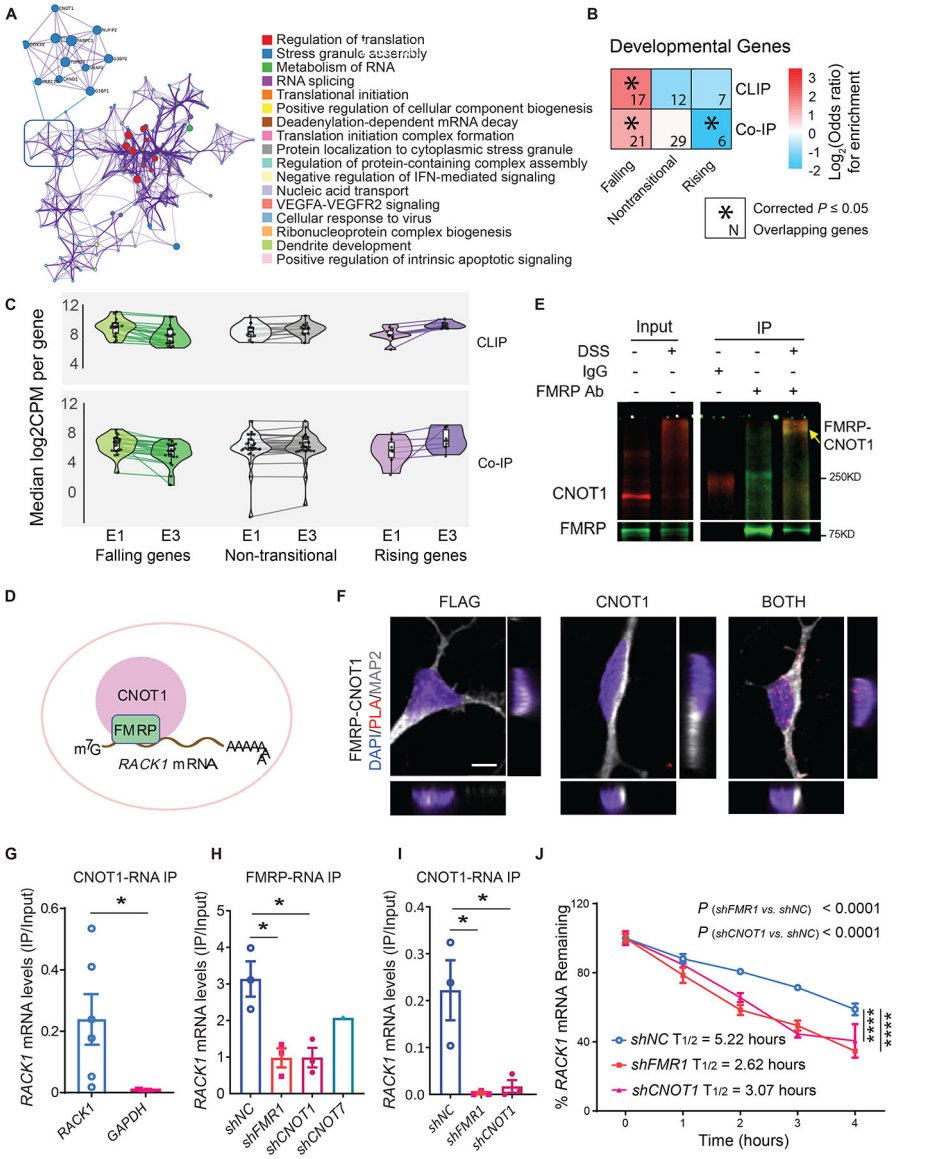

Figure 5. FMRP interacts with CNOT1 to regulate RACK1 expression

(A) Top: protein-protein interaction network of FMRP interactors in human mature neurons. Bottom: the similarity network of enriched terms of these FMRP interactors. Nodes are enriched terms. Colors represent the enrichment clusters.

(B) Gene set enrichment analyses (two-sided Fisher's exact test, FET) of FMRP targets and interactors in human mature neurons against genes with distinct expression trajectories during early human cortical development.

(C) Expression level (median $\log_2$ counts per million across samples) of FMRP targets (top) and interactors (bottom) in human cortex from BrainVar in developmental epoch 1 (10–19 post-conception weeks) and epoch 3 (6 months-20 years), for genes with falling (green), non-transitional (gray) and rising (purple) trajectories.

(D) Model for FMRP-CNOT1 interaction in regulating RACK1 expression in human neurons during embryonic development.

(E) CoIP-WB for detecting protein-protein interaction of FMRP and CNOT1 using FMRP antibody as a bait in human neurons.
(F) PLAs for detecting protein-protein interaction of FMRP and CNOT1 in proximity *in situ* in human neurons.
(G) RNA immunoprecipitation followed by quantitative PCR (RNA-IP-qPCR) to detect binding of CNOT1 to *RACK1* mRNA in human mid-fetal cortical tissue.
(H) RNA-IP-qPCR for detecting binding of FMRP and *RACK1* mRNA in human 293 cells infected with LV-*shFMR1*, LV-*shCNOT1* and LV-*shCNOT7*.
(I) RNA-IP-qPCR for detecting binding of CNOT1 and *RACK1* mRNA in human 293 cells infected with LV-*shFMR1*, LV-*shCNOT1*.
(J) Assessment of *RACK1* mRNA stability in LV-*shFMR1* and LV-*shCNOT1* infected HEK293 cells treated with transcriptional inhibitor actinomycin D. The amount of *RACK1* mRNA was quantified using real-time PCR. Half-life of decay was calculated after transforming data to ln.
Two-tailed Student's test in (G). One-way ANOVA in (H and I). Two-way ANOVA with Bonferroni post hoc test in (J). Mean ± SEM G: N = 6, H-J n = 3 except for shCNOT7 in H (n = 1). p value, *p < 0.05 and ****p < 0.0001
See also Figure S6 See also Table S1 for detailed information on cell lines used

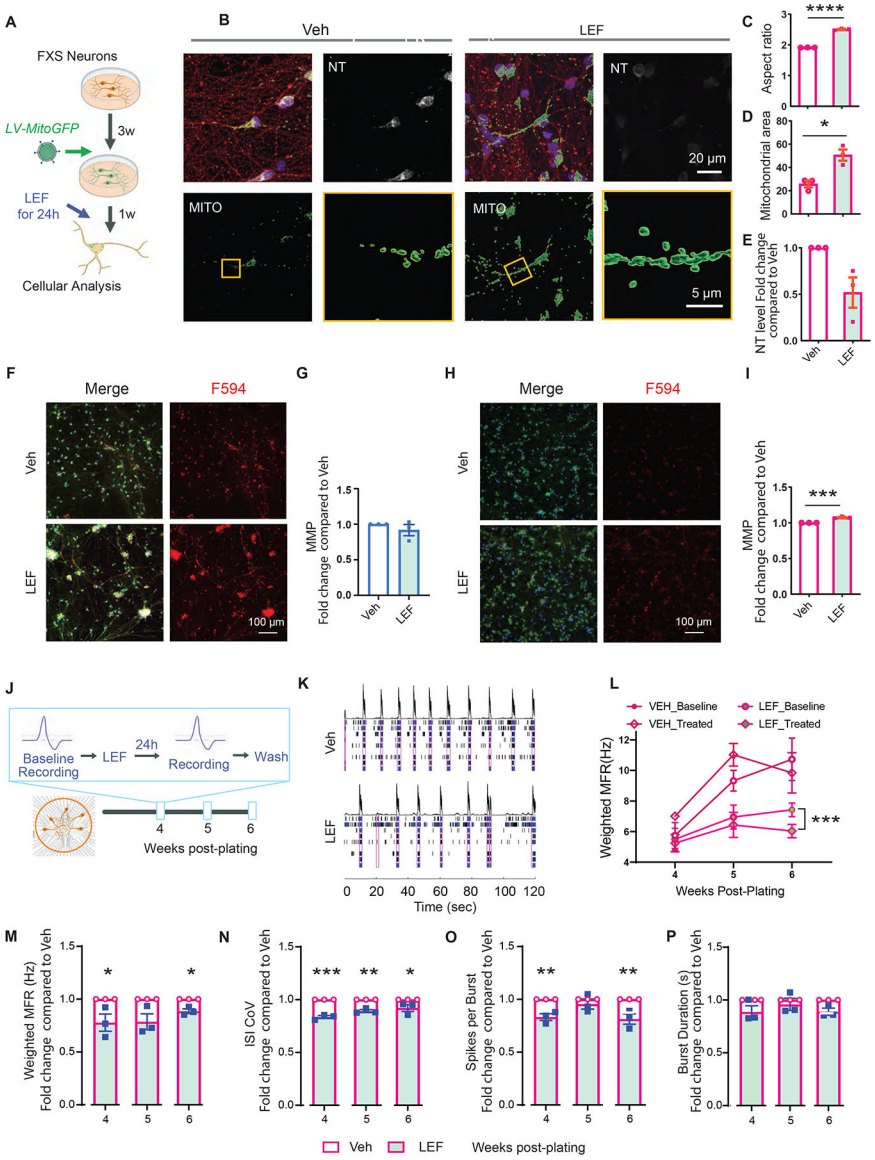

Figure 6. Mitochondrial protector rescues mitochondrial deficits and hyperexcitability in human FXS neurons

(A-G) Mitochondrial protector rescues mitochondrial deficits in human FXS neurons.

(A) Experimental scheme for assessing LEF effects on mitochondria in FXS neurons.

(B) Representative confocal images of leflunomide (LEF) or vehicle (Veh)-treated human FXS neurons stained with Mito-GFP (MITO, green), TUJ1 (red), and NT (white) and 3D reconstruction of mitochondria (in yellow frame).

(C-E) Quantification of mitochondrial aspect ratio (C), mitochondrial area (D), and NT level (E, p = 0.0981) of FXS neurons treated with LEF.

(F, G) Representative images (F) and quantification (G) of MMP of control neurons treated with LEF.

(H, I) Representative images (H) and quantification (I) of MMP of FXS neurons treated with LEF.

(J-P) Mitochondrial protector alleviates hyperexcitability of human FXS neurons.

(J) Schematics for assessing LEF effects on hyperexcitability of FXS neurons. At 4, 5, and 6 weeks post-plating, neurons were recorded by MEA before treatment (Baseline Recording) and then treated with LEF for 24 hours followed by a second MEA recording (Treated Recording). After measurement, the medium was changed (Wash).

(K) Representative raster plots showing 120s of activity of FXS neurons after 24-hour treatment of LEF or Veh.

(L) Quantification of weighted MFR of FXS neurons measured at baseline and after either VEH or LEF treatment at week 4, 5, and 6 weeks post-plating.

(M-P) Quantification of weighted MFR (M), ISI CoV (N), number of spikes per burst (O) and burst duration (P) of FXS neurons. The values of treatment (Veh or LEF) were normalized to their own baseline measurement first and then LEF treatment was normalized to Veh for visualization.

Two-tailed Student's test in (C and D). Two-tailed Student's test with Welch's correction in (E, G, J).

Two-way ANOVA with Bonferroni post hoc test in (L-P). Mean ± SEM from n = 3 independent differentiations *p < 0.05, **p < 0.01, and ***p < 0.001

See also Figure S7 and Table S1 for detailed information on cell lines used

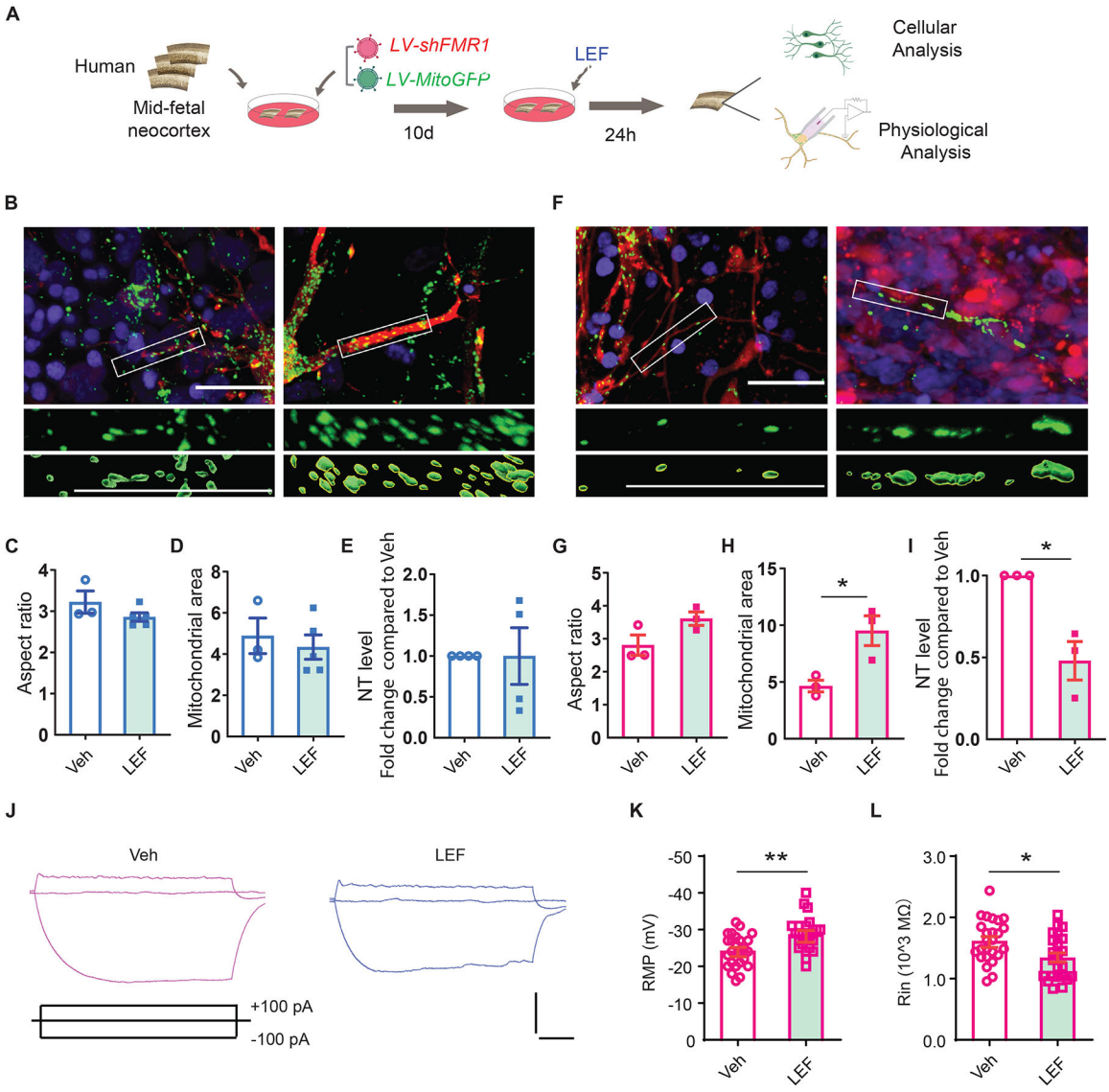

Figure 7. Mitochondrial protector rescues mitochondrial deficits and hyperexcitability of FMRP-deficient neurons in cortical tissue

(A) Experimental scheme for assessing LEF effects on mitochondria in human FMRP-deficient mid-fetal cortical neurons. Schematics was adapted from[64]

(B-E) Mitochondrial protector does not affect mitochondria in Ctrl neurons in human mid-fetal cortical tissue.

(B) Representative confocal images of LEF-treated LV-*shNC*-infected human fetal cortex stained with MitoGFP (green), mCherry (red), and DAPI followed by 3D reconstruction of mitochondria.

(C-E) Quantification of mitochondrial aspect ratio (C), mitochondrial area (D) and NT level (E) of *LV-shNC* infected neurons on human fetal cortex treated with 24-hour LEF.

(F-I) Mitochondrial protector rescues mitochondrial deficits in FMRP-deficient (FMRP-KD) neurons in human mid-fetal cortical tissue.

(F) Representative confocal images of 24-hour LEF (12.5 μM)-treated LV-*shFMR1*-infected human fetal cortex stained with MitoGFP (green), mCherry (red), and DAPI followed by 3D reconstruction of mitochondria.

(G-I) Quantification of mitochondrial aspect ratio (G, $p = 0.0946$), mitochondrial area (H) and NT level

(I) of *LV-shFMR1* infected neurons on human fetal cortex treated with 24-hour LEF.

(J-L) Whole-cell recording analysis of FMRP-deficient neurons on human mid-fetal cortex.

(J) Example of potential trains upon current injections from shRNA-mCherry neurons. Scale bars showing amplitude (25 mV) and time (0.1 sec).

(K, L) Quantification of RMP (K) and R_{in} (L). Veh: n = 25, LEF: n=23 cells from 3 biological replicates.

Two-tailed Student's test in (C, D, G, H, K, L). Two-tailed Student's test with Welch's correction (E and I). Mean ± SEM from N=3 biological replicates. *$p < 0.05$, **$p < 0.01$. See also Table S1 for detailed information on cell lines used

KEY RESOURCES TABLE

REAGENT or RESOURCE	SOURCE	IDENTIFIER
Antibodies		
Anti-FLAG	Sigma-Aldrich	Cat# F1804, RRID: AB_262044
Anti-ATP5B	Proteintech	Cat# 17247-1-AP, RRID: AB_2061878
Anti-CLTC	Proteintech	Cat# 66487-1-Ig, RRID: AB_2881852
Anti-CNOT1	Proteintech	Cat# 14276-1-AP, RRID: AB_10888627
Anti-CRMP1	Proteintech	Cat# 10317-1-AP, RRID:AB_2085347
Anti-DYNC1H1	Proteintech	Cat# 12345-1-AP, RRID:AB_2261765
Anti-FMRP	Abcam	Cat# ab17722, RRID:AB_2278530
Anti-FMRP	Santa Cruz Biotechnology	Cat# sc-101048, RRID:AB_1122951)
Anti-GAPDH	Thermo Fisher Scientific	Cat# MA5-15738, RRID:AB_10977387
Anti-GFP	Invitrogen	Cat# A10262
Anti-HSP90AA1	Proteintech	Cat# 13171-1-AP, RRID:AB_2120924)
Anti-HSP90AB1	Proteintech	Cat# 11405-1-AP, RRID:AB_2121207
Anti-KIF5C	Proteintech	Cat# 25897-1-AP, RRID:AB_2880288
Anti-MAP2	Sigma-Aldrich	Cat# M1406, RRID:AB_477171
Anti-mCherry	Thermo Fisher Scientific	Cat# M11217, RRID:AB_2536611
Anti-Nanog	Stemgent	Cat# 09-0020, RRID:AB_2298294
Anti-NeuN	Cell Signaling Technology	Cat# 24307, RRID:AB_2651140
Anti-Nitrotyrosine	Santa Cruz Biotechnology	Cat# sc-32757, RRID:AB_628022
Anti-Oct 3/4	Santa Cruz Biotechnology	Cat# sc-5279, RRID:AB_628051
Anti-PGC1a	Abcam	Cat# ab54481, RRID:AB_881987
Anti-PRPF8	Proteintech	Cat# 11171-1-AP, RRID:AB_2171179
Anti-RACK1	Proteintech	Cat# 27592-1-AP, RRID:AB_2880917
Anti-SATB2	Abcam	Cat# ab92446, RRID:AB_10563678
Anti-Sox2	R&D Systems	Cat# AF2018, RRID:AB_355110
Anti-SPTAN1	Santa Cruz Biotechnology	Cat# sc-48382, RRID:AB_2194351
Anti-SPTBN1	Proteintech	Cat# 19722-1-AP, RRID:AB_10638469
Anti-TUBB3	Biolegend	Cat# 802001, RRID:AB_2564645
Anti-TUBB3	Promega	Cat# G7121, RRID:AB_430874
Anti-8-oxoG	Abcam	Cat# ab206461
Bacterial and virus strains		
LV-*shNC*-mCherry	Guo, Y. *et al.* 2023[22]	N/A
LV-*shFMR1-mCherry*	Guo, Y. *et al.* 2023[22]	N/A
LV-*shNC-BFP*	This paper	N/A
LV-*shRACK1-BFP*	This paper	N/A
LV-*shATP5B-BFP*	This paper	N/A
LV-*shDYNC1H1-BFP*	This paper	N/A

REAGENT or RESOURCE	SOURCE	IDENTIFIER
LV-*shKIF5C-BFP*	This paper	N/A
LV-*shHSP90AA1-BFP*	This paper	N/A
LV-*shHSP90AB1-BFP*	This paper	N/A
LV-*shSPTAN1-BFP*	This paper	N/A
LV-*shSPTBN1-BFP*	This paper	N/A
LV-*shMAP2-BFP*	This paper	N/A
LV-*shCLTC-BFP*	This paper	N/A
LV-*shCRMP1-BFP*	This paper	N/A
LV-*shPRPFB-BFP*	This paper	N/A
LV-*shCNOT1-BFP*	This paper	N/A
LV-*RACK1-BFP*	This paper	N/A
LV-*hSyn-Mito*-cGFP	Shen, M. *et al.* 2019[7]	N/A
Chemicals, peptides, and recombinant proteins		
DMEM/F12	Thermo Fisher Scientific	Cat# 11330032
Neurobasal	Thermo Fisher Scientific	Cat# 21103049
Knockout Serum Replacement (KOSR)	Thermo Fisher Scientific	Cat# 10828028
Antibiotic-Antimycotic	Thermo Fisher Scientific	Cat # 15240062
Dispase II	Thermo Fisher Scientific	Cat# 17105041
Collagenase, Type IV	Thermo Fisher Scientific	Cat# 17104019
StemPro™ Accutase	Thermo Fisher Scientific	Cat# A1110501
TrypLE Express Enzyme	Thermo Fisher Scientific	Cat# 12605010
B-27 (without vitamin A)	Thermo Fisher Scientific	Cat# 12587020
Glutamax	Thermo Fisher Scientific	Cat# 35050061
L-glutamine	Thermo Fisher Scientific	Cat# 25030081
Laminin Mouse Protein, Natural	Thermo Fisher Scientific	Cat# 23017015
MEM NEAA	Thermo Fisher Scientific	Cat# 11140050
SYTO Deep Read Nucleic Acid Stain, for live cells	Thermo Fisher Scientific	Cat# S34900
NucBlue™ Live ReadyProbes Reagent (Hoechst 33342)	Thermo Fisher Scientific	Cat# R37605
SB431542	Biogems	3014193
puromycin	InvivoGen	Cat# ant-pr-1
LDN-193189	Selleck Chemicals	Cat# S2618 CAS: 1062368-24-4
XAV 939	Tocris	Cat# 3748 CAS: 284028-89-3
Y-27632	Tocris	Cat# 1254 CAS:129830-38-2
Matrigel	Corning	Cat# 354248
Glucose	Dot Scientific	DSG32040
Recombinant Human/Murine/Rat BDNF	Peprotech	Cat# 450-02
Recombinant Human GDNF	Peprotech	Cat# 450-10
DMEM, High Glucose	Sigma-Aldrich	Cat# D5796
L-ascorbic acid	Sigma-Aldrich	Cat# A8960 CAS: 1713265-25-8

REAGENT or RESOURCE	SOURCE	IDENTIFIER
Cyclic AMP (cAMP)	Sigma-Aldrich	Cat# D0260 CAS: 241-059-4
γ-Secretase Inhibitor XXI, Compound E	Sigma-Aldrich	Cat# 565790 CAS: 209986-17-4
2-mercapto-ethanol	Sigma-Aldrich	Cat# M6250 CAS: 60-24-2
Dimethyl sulfoxide (DMSO)	Sigma-Aldrich	Cat# D2650 CAS: 67-68-5
Poly-L-ornithine	Sigma-Aldrich	Cat# P4638 CAS: 27378-49-0
Uridine	Sigma-Aldrich	Cat# U3003 CAS: 58-96-8
Alpha-tocopherol (vitamin E)	Sigma-Aldrich	Cat# T3251-25G CAS: 10191-41-0
Cholecalciferol (Vitamin D3)	Sigma-Aldrich	Cat# C9756-5G CAS: 67-97-0
CoEnzyme Q10 (CoQ10)	Sigma-Aldrich	Cat# C9538-100MG CAS: 303-98-0
Curcumin	Sigma-Aldrich	Cat# C1386-10G CAS: 458-37-7
Docosahexainoic acid (DHA)	Sigma-Aldrich	Cat# D2534-100MG CAS: 6217-54-5
Epigallocatechin-3-gallate (EGCG)	Sigma-Aldrich	Cat# Y0001936 CAS: 989-51-5
Folic Acid (Vitamin B9)	Sigma-Aldrich	Cat# F7876-10G CAS: 1207282-75-4
Ginseng*	Sigma-Aldrich	Cat# G7253-5G
Idebenone	Sigma-Aldrich	Cat# I5659-25MG CAS: 58186-27-9
Leflunomide	Sigma-Aldrich	Cat# PHR1378-1G CAS: 75706-12-6
M1	Sigma-Aldrich	Cat# 475859-25MG
Mdivi-1	Sigma-Aldrich	Cat# M0199-5MG CAS: 338967-87-6
Melatonin	Sigma-Aldrich	Cat# M5250-1G CAS: 73-31-4
Mitoquinone (MitoQ)	MedKoo Biosciences	Cat# 317102 CAS: 845959-50-4
MitoTEMPO	Sigma-Aldrich	Cat# SML0737-5MG CAS: 1334850-99-5
N-acetyl-cysteine	Sigma-Aldrich	Cat# A7250-10G CAS: 616-91-1
Retinoic Acid (Vitamin A)	Sigma-Aldrich	Cat# R2625-500MG CAS: 302-79-4
Teriflunomide	Sigma-Aldrich	Cat# SML0936-10MG CAS: 163451-81-8
DSS (disuccinimidyl suberate)	Thermo Fisher Scientific	Cat#: 21555 CAS: 68528-80-3
FCCP, mitochondrial oxidative phosphorylation uncoupler	abcam	ab120081 CAS: 370-86-5
Critical commercial assays		
Duolink® In Situ Detection Reagents Red	Sigma-Aldrich	DUO92008
Duolink® In Situ PLA® Probe Anti-Mouse MINUS	Sigma-Aldrich	DUO92004
Duolink® In Situ PLA® Probe Anti-Rabbit PLUS	Sigma-Aldrich	DUO92002
JC-10 Mitochondrial Membrane Potential Assay Kit (Microplate)	Abcam	ab112134
CellTiter-Glo® 2.0 Cell Viability Assay	Promega	G9242
NAD/NADH-Glo™ Assay	Promega	G9072
Deposited data		
CLIP-seq	Gene Expression Omnibus (GEO)	GSE217284
Co-IP-MS	This paper	Table S4
Experimental models: Cell lines		

REAGENT or RESOURCE	SOURCE	IDENTIFIER
HEK293T	ATCC	https://www.atcc.org/
WC053i-FX08-25	This paper	
WC007i-FX13-2	WiCell	RRID: CVCL_EJ78
WC005i-FX11-7	WiCell	RRID: CVCL_EJ76
H1 KO (WAe001-A-50)	WiCell; Published in Li *et al.* (2020)[24] WiCell http://www.wicell.org	RRID: CVCL_C0CC
GM1(GM00498-4)	Coriell Institute	RRID: CVCL_7290
WC031i-5907-6 (WISCi008-C)	WiCell	RRID: CVCL_VF57
WC032i-6007-1 (WISCi009-A)	WiCell	RRID: CVCL_VF58
H9 (WA09)	WiCell	RRID: CVCL_9773
H1 (WA01)	WiCell	RRID: CVCL_9771
H13 (WA13)	WiCell	RRID: CVCL_9774
H1-*FMR1*-FLAG (WAe001-A-51)	WiCell; Published in Li *et al.* (2020)[24] WiCell http://www.wicell.org	RRID: CVCL_C0CD
H13-*FMR1*-FLAG		Published in Li *et al.* (2020)[24]
GM1-*FMR1* FLAG		Published in Li *et al.* (2020)[24]
Experimental models: Organisms/strains		
Human mid-fetal cortical tissues	Birth Defects Research Laboratory (BDRL) at the University of Washington	N/A
Macaque mid-fetal cortical tissues	Wisconsin National Primate Research Center, University of Wisconsin-Madison	N/A
Mouse: C57BL/6J	Jackson Laboratory	RRID:IMSR_JAX:000664
Mouse: Fmr1-KO	Jackson Laboratory	RRID:IMSR_JAX:004624
Oligonucleotides		
Please see table S1B	This paper	table S1C
Recombinant DNA		
pLV-*shNC*-mCherry	Guo, Y. *et al.* 2023[22]	N/A
pLV-*shFMR1-mCherry*	Guo, Y. *et al.* 2023[22]	N/A
pLV-*shNC-BFP*	This paper	N/A
pLV-*shRACK1-BFP*	This paper	N/A
pLV-*shATP5B-BFP*	This paper	N/A
pLV-*shDYNC1H1-BFP*	This paper	N/A
pLV-*shKIF5C-BFP*	This paper	N/A
pLV-*shHSP90AA1-BFP*	This paper	N/A
pLV-*shHSP90AB1-BFP*	This paper	N/A
pLV-*shSPTAN1-BFP*	This paper	N/A
pLV-*shSPTBN1-BFP*	This paper	N/A
pLV-*shMAP2-BFP*	This paper	N/A

REAGENT or RESOURCE	SOURCE	IDENTIFIER
pLV-*shCLTC-BFP*	This paper	N/A
pLV-*shCRMP1-BFP*	This paper	N/A
pLV-*shPRPFB-BFP*	This paper	N/A
pLV-*shCNOT1-BFP*	This paper	N/A
pLV-*shCNOT7-BFP*	This paper	N/A
pLV-*RACK1-BFP*	This paper	N/A
pLV-*hSyn-Mito*-cGFP	Shen, M. *et al.* 2019[7]	N/A
Software and algorithms		
Prism (v10)	GraphPad	https://www.graphpad.com
ImageJ	National Institute of Health	https://imagej.nih.gov/ij/docs/guide/user-guide.pdf
NIS-Elements	Nikon	https://www.nikoninstruments.com/Products/Software
ImageStudio (v5.2)	Li-Cor	https://www.licor.com/bio/products/software/image_studio/
FASTX Toolkit (v0.0.14)	Hannon Lab	http://hannonlab.cshl.edu/fastx_toolkit/
cutadapt (v1.7.1)	Martin Lab	http://cutadapt.readthedocs.io/en/stable/
STAR (v2.5.3a)	Gingeras Lab	https://github.com/alexdobin/STAR
R (v3.5.1)	The R Foundation	https://www.r-project.org/
DESeq2 (v1.20.0)	Anders Lab	https://bioconductor.org/packages/release/bioc/html/DESeq2.html
RSeQC (v2.6.4)	Li Lab	http://rseqc.sourceforge.net/
clusterProfiler (v3.4.4)	Yu Lab	http://bioconductor.org/packages/release/bioc/html/clusterProfiler.html
VennDiagram (v1.6.17)	Chen Lab	https://cran.r-project.org/web/packages/VennDiagram/index.html
LIMMA (v3.35.15)	Smyth Lab	https://bioconductor.org/packages/release/bioc/html/limma.html
Cytoscape (v3.5.1)	Cytoscape Consortium	http://www.cytoscape.org/
IGV (v2.4.5)	Broad Institute	https://software.broadinstitute.org/software/igv/
pClamp 10.4	Molecular Devices	RRID:SCR_011323
CLIPer	Van Nostrand 2016[69]	
ANYmaze	Stoelting	https://www.stoeltingco.com/anymaze.html
GraphPad	GraphPad	RRID:SCR_000306
Columbus (v2.9.1)	PerkinElmer	https://www.perkinelmer.com/product/image-data-storage-and-analysis-system-columbus
AxIS Navigator (v3.7.1)	Axion Biosystems	https://www.axionbiosystems.com/products/mea/mea-software
AxIS Metric Plotting Tool (v2.5.0)	Axion Biosystems	https://www.axionbiosystems.com/products/mea/mea-software

REAGENT or RESOURCE	SOURCE	IDENTIFIER
MetaXpress (v6.7.2.290)	Molecular Devices	https://www.moleculardevices.com/products/cellular-imaging-systems/acquisition-and-analysis-software/metaxpress RRID:SCR_016654